Circadian PERIOD complex regulates TC-DSB repair through anchoring to the nuclear envelope.

Benjamin Le Bozec[1], Laure Guitton-Sert[1], Sarah Collins[1], Vincent Rocher[1], Emmanuelle Guillou[1], Charlotte Payrault[1], Coline Arnould[1], Aude Guénolé[1], Marion Aguirrebengoa[2], Anne-Laure Finoux[1], Thomas Mangeat[3], Nadine Puget[1*] and Gaëlle Legube[1,4*]

1. *MCD, Centre de Biologie Intégrative (CBI), CNRS, Université de Toulouse, UT3, 31062 Toulouse, France*
2. *BigA, NGS data analysis facility, Centre de Biologie Intégrative (CBI), CNRS, Université de Toulouse, UT3, 31062 Toulouse, France*
3. *LITC Core Facility, Centre de Biologie Intégrative (CBI), CNRS, Université de Toulouse, UT3, 31062 Toulouse, France*
4. *Lead author*

* Corresponding authors: gaelle.legube@univ-tlse3.fr, nadine.puget1@univ-tlse3.fr

Running title: Circadian regulation of TC-DSB repair

Abstract

Repair of DNA Double-Strand Breaks (DSBs) produced in transcriptionally active chromatin occurs through a poorly characterized pathway called Transcription-Coupled DSB repair (TC-DSBR). Here, using a screening approach scoring multiple outputs in human cells, we identified the PER complex, a key module ensuring circadian oscillations, as a novel TC-DSBR player. Circadian rhythm has been involved in repair of UV-induced DNA damage but very little is known about its contribution to DSB repair pathways. We show that the PER complex is recruited at DSBs occurring in transcribed loci and we further found that the core protein PER2 contributes to targeting TC-DSBs at the nuclear envelope (NE) and to foster RAD51-mediated repair. PER2 deficiency triggers decreased DSB anchoring to the NE, resulting in an increase of DSB clustering and translocation frequency. In agreement, we found that the circadian clock also regulates DSB anchoring to the NE and RAD51 assembly. In conclusion, our study provides a direct link between the circadian rhythm and the response to DSBs occurring in active genes, opening new therapeutic strategies for chemotherapies based on topoisomerase poisons that mostly induce DSBs in active loci.

Main

DNA Double-Strand breaks (DSBs) are among the most toxic lesions that occur on the genome, given their potential to elicit large chromosomal rearrangements. Genome-wide mapping of DSBs established that endogenous DSBs mostly appear in transcriptionally active chromatin (TC-DSBs)[1–4]. While global genome DSB repair (GG-DSBR) mechanisms have been well characterized, a transcription-coupled arm of DSB repair (TC-DSBR) has only recently been identified[5]. TC-DSBR entails the transcriptional repression of the damaged genes via ATM and DNA-PK dependent mechanisms[5,6] which is necessary for the initiation of resection. In G2, TC-DSBs are further channeled to repair by HR thanks to transcription-associated chromatin marks such as H3K36 trimethylation and H4 acetylation for instance[7–9], in a manner that also depends on Senataxin (SETX)-dependent removal of RNA:DNA hybrids that accumulate at TC-DSBs. In G1, TC-DSB repair is delayed[10] and may rely on CSB and RAD52[11]. The persistent TC-DSBs in G1 are prone to cluster in large subnuclear structures[10], that we recently identified as a novel, DSB-induced, chromatin compartment, called the D-compartment[12] and which enhances translocation frequency. Additionally, when occurring on human ribosomal DNA, TC-DSBs are physically relocated at the nucleolar periphery where they can contact invaginations of the Nuclear Envelope (NE)[13]. Whether this also occurs at RNAPII-transcribed damaged loci is yet unknown, although such NE targeting of persistent DSBs has been previously reported in *Drosophila* and *S. Cerevisiae*[14–17].

Multi-output screen to identify new TC-DSBR factors

In search of novel TC-DSBR players, we performed a siRNA library screen scoring multiple outputs (Fig. 1a) in the well-characterized human DIvA cell line, where 174 DSBs are induced in a temporally controlled manner at annotated positions, a large fraction of which

occur in RNAPII-enriched (transcribed) loci[18,19]. The siRNA library comprised of 130 candidate proteins, previously found to be preferentially associated with the SMC1 cohesin subunit post-DSB induction[13]. The screen was designed to quantify the effect of candidate protein depletion on 1) γH2AX foci intensity using high-content imaging, 2) cell survival using a cell proliferation assay, 3) chromosome rearrangement frequency using quantitative PCR and 4) DSB clustering using high content microscopy (Fig. 1a, Extended Data Fig. 1a). A positive control siRNA against SETX, previously involved in TC-DSBR[20,21], triggered as expected increased γH2AX foci intensity, translocation frequency and DSB clustering as well as decreased cell proliferation (Fig. 1b-e, red bars). We further validated our screening dataset with the candidate protein Periphilin (PPHLN1, Fig. 1b-e, green bars), an H3K9me3 reader of the HUSH complex that we previously involved in ribosomal DNA DSB repair[13]. Similar to the screen results, depletion of PPHLN1 triggered an increase in γH2AX foci intensity and translocation frequency, and a decreased clonogenic potential (Extended Data Fig. 1b-e).

Importantly, two-parameter correlations established that γH2AX intensity was inversely correlated with cell survival but positively correlated with translocation frequency (Fig. 1f-g), consistent with a decreased repair capacity respectively impairing cell proliferation and promoting genome rearrangement. Moreover, increased DSB clustering positively correlated with translocation frequency (Fig. 1h), and increased translocation inversely correlated with cell survival (Fig. 1i) in agreement with previous work[12,22]. Altogether, results from our siRNA screen establish that TC-DSBR deficiency severely affects cell survival and further confirm the relationship between DSB clustering and genome rearrangement as recently reported[12,22].

The circadian clock PERIOD complex contributes to TC-DSB repair.

84 Interestingly, among the candidate proteins whose depletion gave similar phenotypes to
85 SETX, we found NONO, SFPQ and DDX5 which all belong to the same complex, the
86 mammalian PERIOD (PER) complex involved in the regulation of the circadian rhythm[23–26].
87 SETX itself belongs to the PER complex[25] and similar outputs were also seen for another
88 candidate, the DDX5-paralog DDX17, both DDX5 and DDX17 being human orthologs of the
89 *Neurospora* PRD1 protein involved in circadian rythmicity[27] and existing as a heterodimer[28].
90 Our screen indicated that the depletion of five distinct proteins within the PER complex
91 triggered increased γH2AX staining, decreased cell survival, increased chromosomal
92 rearrangement and increased DSB clustering (Fig. 1b-e, blue bars). The circadian clock is
93 molecularly controlled by the BMAL1/CLOCK transcriptional activator complex, which
94 regulates the transcription of thousands of genes. Among those, the PER-CRY transcriptional
95 repressor can downregulate BMAL1/CLOCK activity, creating a negative transcriptional
96 feedback loop that ensures circadian oscillations[29]. In order to directly investigate whether the
97 core clock components of the PER complex play a role in TC-DSBR, we depleted PER1 and
98 PER2 proteins (Extended Data Fig. 2a). As found for DDX17, NONO, DDX5 and SETX (Fig.
99 1b), PER1 and PER2 knockdown increased γH2AX foci intensity following DSB induction in
100 DIvA cells (Fig. 2a) with no major changes in cell cycle distribution (Extended Data Fig. 2b).
101 In agreement, PER2-depleted cells also displayed elevated γH2AX levels detected by chromatin
102 immunoprecipitation (ChIP) around DSBs (Fig. 2b). Moreover, PER1 and PER2 depletion
103 increased translocation frequency (Fig. 2c) and impaired cell survival following induction of
104 TC-DSBs in DIvA cells (Fig. 2d, Extended Data Fig. 2c) as similarly found for DDX17, NONO,
105 SETX and DDX5 (Fig. 1c-d; Fig. 2c-d; Extended Data Fig. 2d). In contrast, depletion of the
106 BMAL1 transcriptional activator had no effect on translocation frequency or cell survival post
107 DSB induction (Fig. 2c-d, Extended Data Fig. 2d). Altogether, these data show that the

108 PERIOD proteins PER1 and PER2, as well as other members of the PER complex, contribute
109 in the response to DSBs induced in transcribed loci.

110 In order to determine whether the function of the PER complex is direct, we assessed the
111 recruitment of PER complex proteins at DSBs using ChIP. PER2, DDX5 and DDX17 all
112 showed significant recruitment at a TC-DSB induced in DIvA cells, while this was not the case
113 for BMAL1 (Fig. 3a). We further performed ChIP-seq against PER2 and BMAL1 in damaged
114 and undamaged DIvA cells. Both proteins displayed the expected pattern on the genome (see
115 examples Extended Data Fig. 3a). Indeed, in absence of DSB induction, BMAL1 was enriched
116 on genomic loci previously identified by BMAL1 ChIP-seq[30] (Extended Data Fig. 3b) and
117 PER2 accumulated at promoters (Extended Data Fig. 3c) as expected for a transcriptional
118 repressor and from previous studies[31]. Moreover, BMAL1-bound genes displayed significant
119 enrichment for the "rhythmic process" GO term (Extended Data Fig. 3d). Post-DSB induction,
120 we interestingly observed that PER2 accumulated at TC-DSBs (see an example Fig. 3b top
121 panel, purple track) but not at a silent locus (Fig. 3b bottom panel), despite equivalent cleavage
122 (BLESS tracks). In contrast, BMAL1 showed no accumulation at DSBs (Fig. 3b, blue tracks).
123 On average, PER2 (left panel) was significantly targeted on ~2kb around DSBs, while BMAL1
124 (right panel) was not (Fig. 3c, Extended Data Fig. 3e).

125 We previously identified a subset of equivalently cleaved DSBs in DIvA cells with two distinct
126 repair behaviors: the Non-Homologous End-Joining (NHEJ)-prone DSBs and the HR-prone
127 DSBs with the latter having a tendency to locate within transcriptionally active loci (*i.e.* TC-
128 DSBs)[8,18]. Importantly, here we found that PER2 preferentially accumulates at HR-prone TC-
129 DSBs compared to NHEJ-prone DSBs (*i.e.* occurring in non-transcribed regions) (Fig. 3d).

130 Thus, in order to establish whether PER2 contributes to repair at HR-prone DSBs, we further
131 investigated the effect of PER1/2 depletion on end-resection, by quantification of single-

132 stranded DNA at various distances from DSBs (Fig. 3e left panel). siRNA depletion of both
133 PER1 and PER2 triggered a moderate, yet significant, decrease of resection (Fig. 3e, right
134 panel), although less pronounced than upon CtIP depletion. Moreover, PER2 depletion
135 triggered a significant decrease in RAD51 binding at TC-DSBs (Fig. 3f). One of the first steps
136 of TC-DSB repair is the transcriptional repression of nearby genes (including the damaged gene
137 itself) which is essential for the proper execution of resection and HR repair[5]. Given that the
138 PER complex is a transcriptional repressor, we envisaged that the PER complex could promote
139 HR repair at TC-DSBs via a role in transcriptional repression. However, RT-qPCR analyses
140 revealed that both PER2 and PER1 are dispensable for this transcriptional repression following
141 DSB induction (Fig. 3g). Altogether these data show that the PER complex is recruited at TC-
142 DSBs where it contributes to resection and fosters RAD51 recruitment, suggesting a direct
143 function in TC-DSBR downstream of transcriptional repression.

144

145 **TC-DSBs are targeted to the nuclear envelope via a SUN1-dependent mechanism.**

146 The nuclear envelope (NE) contributes to the regulation of the circadian clock[32] and PER
147 proteins have recently been involved in the physical targeting of clock-regulated genes to the
148 NE in *Drosophila*[33]. Of interest, persistent DSBs were previously found to be relocated at the
149 NE in yeast[14,16,17,34], as were heterochromatic (HC) DSBs in *Drosophila* in order to complete
150 HR[15,35]. While in mammalian cells, physical relocation of DSBs to the NE has not yet been
151 documented, we previously observed that ribosomal DNA DSBs can contact NE invaginations
152 inside the nucleoplasm[13]. Hence, we set out to determine whether TC-DSBs could be targeted
153 to the NE. As a first approach, we performed fixed and live super-resolution imaging using
154 Random Illumination Microscopy (RIM)[36]. We observed that γH2AX foci can establish close
155 contact with LaminB1 filaments (Extended data 4a). Live imaging after DSB induction in DIvA

156 cells expressing 53BP1-GFP and mCherry-LaminB1, showed that such interactions between
157 DSBs and nuclear lamina were rapidly established (<60s) and transient (Fig. 4a and
158 Supplementary Videos 1-4). Contacts between repair foci and the nuclear lamina were further
159 confirmed by Proximity Ligation Assay (PLA) performed between LaminB1 and 53BP1 (Fig.
160 4b) or between γH2AX and LaminB1 (Extended Data Fig. 4b). In agreement, ChIP against
161 LaminB1 (Extended Data Fig. 4c, top panel) also revealed that, in DIvA cells post-DSB
162 induction, LaminB1 occupancy increased at TC-DSBs in contrast to a DSB induced in a silent
163 locus and repaired by NHEJ (Fig. 4c). Taken together, these data suggest that TC-DSBs can be
164 physically relocated at the NE in human cells.

165 Interestingly, we and others previously reported a function for SUN domain containing-
166 proteins, which are components of the Inner Nuclear Membrane (INM), in DSB mobility in
167 mammals[10,37]. Moreover, SUN proteins orthologs in yeast and *Drosophila* (respectively Mps3,
168 and Koi/Spag4) were also found as DSB anchoring points in the NE[15–17]. We thus investigated
169 the potential involvement of the two main SUN proteins in mammals, SUN1 and SUN2, in
170 targeting TC-DSBs to the NE. Interestingly, ChIP against SUN proteins (Extended Data Fig.
171 4c, middle and bottom panels) revealed that, upon damage, SUN1 displayed enrichment at TC-
172 DSBs compared to NHEJ-DSBs (Extended Data Fig. 4d, top panel). Surprisingly, SUN2 rather
173 showed decreased occupancy post-DSB induction (Extended Data Fig. 4d, bottom panel),
174 suggesting that TC-DSBs are specifically interacting with SUN1 and not SUN2. To further
175 investigate SUN protein recruitment at DSBs, we performed ChIP-seq against SUN1 and SUN2
176 before and after DSB induction in DIvA cells. Visual inspection and peak calling on SUN1 and
177 SUN2 ChIP-seq datasets revealed that in undamaged conditions, both proteins are enriched on
178 genes (Extended Data Fig. 4e-f), accumulated at promoters (Extended Data Fig. 4g) and largely
179 overlapped on the genome (Extended Data Fig. 4h). Of interest, post-DSB induction, SUN1
180 (purple track), was recruited on approximately 1kb around the break, while SUN2 rather

181 displayed eviction (blue track) (see an example Fig. 4d top panel, and average profiles at all
182 DSBs Fig. 4e). Both SUN1 recruitment and SUN2 eviction at DSBs were statistically
183 significant when compared to random, undamaged genomic positions (Extended Data Fig. 4i).
184 Of note, as observed for PER2, SUN1 was specifically recruited at a TC-DSB (Fig. 4d top
185 panel) but not at a DSB induced in a silent locus (Fig. 4d bottom panel). We then performed
186 3D-super resolution imaging by RIM to detect SUN1 and SUN2. Both proteins localized to the
187 NE and displayed punctuated patterns (Extended Data Fig. 4j-k). Co-staining with γH2AX
188 enabled the detection of a significant colocalization (ICQ) with SUN1, but not with SUN2 (Fig.
189 4f). Van Steensel Cross-correlation function (CCF) analysis showed non-random overlap
190 between γH2AX foci and SUN1 while non-random exclusion was observed between γH2AX
191 foci and SUN2 (Fig. 4g, see examples on left panels, and quantification on the right panels).

192 Altogether these data suggest that in DIvA cells, TC-DSBs are physically targeted to the NE
193 through an interaction with SUN1 and not SUN2. In order to determine whether NE-targeting
194 of TC-DSBs is functionally relevant, we further determined the consequence of the depletion
195 of SUN-domain proteins (Extended Data Fig. 4l) on cell survival and translocations frequency.
196 Interestingly, depletion of SUN1 decreased cell survival post-DSB induction which correlated
197 with an increased translocation rate (Fig. 4h-i). Of note, this was not the case when depleting
198 SUN2, in agreement with the absence of SUN2 recruitment at DSBs. SUN2 depletion actually
199 triggered an opposite behaviour, decreasing translocation frequency and increasing cell survival
200 post DNA damage (Fig. 4H-I), suggesting that SUN1 and SUN2 competition for inclusion in
201 the NE may regulate TC-DSB docking at the NE. Taken altogether, these data indicate that,
202 similarly to HC breaks in *Drosophila* and persistent breaks in yeast, TC-DSBs also display
203 targeting to the NE in mammalian cells, in a manner that depends on SUN1.

204

205 **PER2 contributes in targeting TC-DSBs to the nuclear envelope**

206 In order to evaluate the consequence of PER2 depletion on TC-DSB targeting at the NE, we
207 performed LaminB1 ChIP in DIvA cells transfected with a PER2 siRNA. Of interest PER2
208 depletion triggered a decrease in LaminB1 recruitment at TC-DSBs (Fig. 5a). Additionally,
209 PER1 or PER2-depleted cells also displayed decreased 53BP1/LMNB1 PLA signal post-DSB
210 induction when compared to PER1/2-proficient cells (siRNA CTRL) (Fig. 5b, Extended Data
211 Fig. 5a). In order to investigate a potential cell cycle dependency for PER2-mediated DSB
212 anchoring to the NE, we then monitored γH2AX/LaminB1 PLA signal combined with EdU
213 incorporation by quantitative high throughput microscopy (Extended Data Fig. 5b). PER2
214 depletion triggered a decreased in PLA foci in G1, S and G2 cells (Fig. 5c). Given our above
215 data on SUN1 recruitment at DSBs (Fig. 4d-g) and the consequences of SUN1 depletion on cell
216 survival (Fig. 4h), we wondered whether SUN1 and PER1/2 would act in the same pathway.
217 Importantly co-depletion of both SUN1 and PER1 or PER2 did not exacerbate the impaired
218 survival observed upon depletion of PER1 or PER2 proteins independently (Fig. 5d). Taken
219 together, these data suggest that the PER core clock components contribute in anchoring TC-
220 DSBs to the NE-embedded SUN1 protein, in human cells.

221

222 **PER2 depletion triggers increased DSB clustering and DSB induced-compartment**
223 **formation.**

224 In mammalian nuclei, Hi-C experiments revealed that chromatin compartmentalizes to form the
225 so-called "A" and "B" compartments, with the B-compartment corresponding to
226 microscopically visible heterochromatin foci[38]. Of interest, both experimental data and
227 computational modeling of chromosome behaviour showed that targeting at the nuclear lamina
228 prevents heterochromatin to coalesce into internal larger nuclear bodies[39]. The current model

229 postulates that upon detachment of chromatin from the NE, phase separation allows multiple
230 HC foci to cluster thus increasing B-compartmentalization. Importantly, we recently reported
231 that upon DSB formation, another chromatin compartment forms, so called the D-compartment
232 (for DSB-induced). This D-compartment, arising via DSB clustering, gathers γH2AX-modified
233 topologically associated domains (TADs) as well as additional undamaged loci, including a
234 subclass of DSB-activated genes[12].

235 Of interest, our siRNA screen indicated that the depletion of NONO, SETX and DDX17 all
236 increased clustering (Fig. 1e) and we found that PER2 contributes in targeting DSBs to the NE
237 (Fig. 5a-c). Hence, we set out to investigate whether PER2 depletion could also increase DSB
238 clustering as a result of DSB detachment from the NE. To address this point, we performed Hi-
239 C experiments before and after DSB induction in PER2-proficient and deficient cells. PER2
240 depletion did not drastically affect chromosome organization in undamaged cells (Extended
241 Data Fig. 5c), nor the overall distribution of A and B compartments (Extended Data Fig. 5d).
242 However, PER2 depletion triggered increased compartmentalization as visualized by increased
243 A-A and B-B interaction, as well as decreased A-B interaction (Extended Data Fig. 5e). This is
244 in agreement with the previously reported role of the PER complex in chromatin anchoring at
245 the NE which would predict an increased compartmentalization upon NE detachment in PER-
246 depleted cells. Upon DSB induction, we could recapitulate our previous finding showing DSB
247 clustering (Extended Data Fig. 5f, arrows). Importantly, PER2 depletion increased DSB
248 clustering as shown on individual events (Fig. 5e, Extended Data Fig. 5f), average aggregate
249 peak analysis (APA) plots of inter-chromosomal or intra-chromosomal DSB-DSB contacts
250 centered on all 80 best-induced DSBs (Fig. 5f, Extended Data Fig. 5g) and box plots quantifying
251 the interactions between DSBs (Fig. 5g). Given previous findings showing that DSB clustering
252 increases translocation rate[12,22,40], these data also agree with the increased translocation
253 frequency observed upon depletion of the PER complex proteins (Fig. 2c).

254 We further computed Chromosomal Eigen Vectors (CEV) using the first PC of Principal
255 Component Analysis (PCA) on differential Hi-C matrices to identify the D-compartment as
256 previously described[12]. As expected, we could recapitulate D-compartment formation upon
257 damage in DIvA cells transfected with a control siRNA (Extended Data Fig. 5h). PER2
258 deficiency did not alter D-compartment detection on chromosomes previously found to display
259 D-compartment (Extended Data Fig. 5h). Of interest, we could observe D-compartment
260 formation on additional chromosomes upon PER2 depletion (Fig. 5h), in agreement with an
261 increased DSB clustering. Taken altogether our data support a model whereby the PER proteins
262 contribute in targeting TC-DSBs to the nuclear lamina, thereby preventing DSB clustering and
263 D-compartment formation.

264

265 **The circadian clock regulates the response to TC-DSBs and their anchoring to the NE.**

266 Given that the PER complex is a core component of the circadian clock, we set out to investigate
267 whether the circadian clock could also regulate the response to TC-DSBs. Dexamethasone
268 treatment synchronized the circadian clock in both U20S and DIvA cells as expected, as
269 assessed by the cycling expression of PER2, BMAL1 and CRY2 (Extended Data Fig. 6a-b).
270 We further monitored γH2AX foci formation in different cell cycle phases, at different time
271 points after dexamethasone-mediated circadian clock synchronization by combining γH2AX
272 staining and EdU labelling, using quantitative high throughput microscopy in DIvA cells. In
273 line with the results obtained with the depletion of PER2 by siRNA, our data indicate that
274 γH2AX foci intensity was increased post-DSB induction during the low-PER2 circadian phase
275 (Fig. 6a, white bars) as compared to the high-PER2 phase (Fig. 6a blue bars). This was
276 independent of the cell cycle phase. Moreover, increased accumulation of γH2AX at TC-DSBs
277 during the low-PER2 phase, was further confirmed by ChIP (Fig. 6b). Of importance the same

278 holds true in S and G2 phases when DSBs were induced using etoposide, a topoisomerase II
279 poison which preferentially induces DSBs in transcribing loci (Extended Data Fig. 6c, top
280 panel). In contrast, the low-PER2 phase was not associated with enhanced γH2AX foci
281 detection when DSBs were induced using bleomycin, a radiomimetic inducing DSBs
282 throughout the genome with no specificity for active loci (Extended Data Fig. 6c, bottom panel).
283 To further reinforce the notion that the low-PER2 phase of the circadian clock impacts TC-DSB
284 repair, we performed circadian clock synchronization and analyzed several outputs that were
285 affected by the depletion of PER2.

286 First, given that our data indicated a role of PER2 in RAD51 assembly at DSBs (Fig. 3f), we
287 assessed RAD51 recruitment using ChIP (Fig. 6c) and RAD51 foci formation using high
288 throughput microscopy (Extended Data Fig. 6e) at different time points after dexamethasone
289 treatment. Both experiments revealed impaired RAD51 recruitment during the low-PER2
290 phase. Second, the circadian clock did not alter transcriptional repression in *cis* to DSBs
291 (Extended Data Fig. 6f) as expected (Fig. 3g). Third, as found using PER2 depletion (Fig. 5a-
292 c), the low-PER2 circadian phase reduced the recruitment of LaminB1 (Fig. 6d) and SUN1
293 (Fig. 6e) to TC-DSBs when monitored by ChIP-qPCR, suggesting that DSB anchoring at the
294 NE is defective when the PER1/2 proteins are expressed at low levels. Fourth, quantitative high
295 throughput microscopy further showed an increase in γH2AX foci area during the low-PER2
296 phase which is in agreement with enhanced DSB clustering (Fig. 6f).

297 We previously reported that, in addition to γH2AX domains, the DSB-induced chromosome
298 compartment (D-compartment) also physically attracts additional loci including some, but not
299 all, DNA damage responsive (DDR) genes, in order to potentiate their activation post-DSB
300 induction[12]. Of interest we found that *RNF19B*, an upregulated DDR gene found within the D-
301 compartment, was significantly more activated post-DSB during the low-PER2 phase when
302 compared to the high-PER2 phase (Fig. 6g). This is in agreement with an increased D-

303 compartment formation in absence of PER2 (Fig. 5e-h). Of importance, this was not the case
304 for other DDR genes which are not targeted to the D-compartment (*PPM1D*, *SLC9A1*)[12], or for
305 other non-induced genes (*LPHN2*, *UTP18*). Altogether these data indicate that the circadian
306 rhythm regulates the repair and signaling of TC-DSBs by controlling their PER2-dependent
307 anchoring to the NE and, therefore, the formation of the D-compartment, further fine-tuning
308 the response to DSBs.

309

310 **Discussion**

311 In this manuscript, we uncovered that the repair of DSBs occurring in transcriptionally active
312 chromatin requires their anchoring to the NE, a process that is under the direct control of the
313 PERIOD complex and is therefore sensitive to circadian oscillations (Fig. 6h).

314 Previous work uncovered that the maintenance of genomic integrity and cancer progression are
315 tightly linked to the circadian clock[41–43]. In general, genes involved in DNA repair pathways
316 are transcriptionally regulated by the circadian clock[42,44–49]. Here we found that in human cells,
317 the PERIOD complex is directly targeted at DSBs. In contrast to a very recent report[50], we did
318 not observe BMAL1 binding at TC-DSBs, although BMAL1 distribution on the genome
319 behaved as expected. This difference may arise from analyzing overexpressed[50] versus
320 endogenous (our study) BMAL1, or from the different DSB-inducible system used in both
321 studies. We found that TC-DSBs occurring in RNAPII-transcribed loci are relocated to the NE,
322 showing for the first time the repositioning of DSBs to the nuclear lamina in humans and
323 expanding the list of DSBs that display this behaviour. This suggests that targeting persistent
324 DSBs to this specific nuclear microenvironment is evolutionary conserved. Here we involved
325 SUN1 as being the TC-DSB docking site at the NE and interestingly SUN1 also displays direct
326 interaction with the Nuclear Pore Complex (NPC), as opposed to SUN2[51,52]. Hence, whether

327 this specific involvement of SUN1 reflects a function for the NPC as a docking point for TC-
328 DSBs will be worth investigating.

329 We found that upon PER1/2 depletion, as well as during the low-PER2 phase, γH2AX level
330 were increased while RAD51 assembly was reduced suggesting a decreased repair capacity. Of
331 interest, in the accompanying paper, the Huertas lab, reports that CRY1 is also recruited at
332 radiation-induced DSBs, where it directly represses resection and HR. Altogether our studies
333 suggest a two-arm control of HR repair during the 24h circadian cycle, with minimum HR
334 occurring at night. Indeed, large transcriptomic surveys, performed in baboon[44] and very
335 recently in human[53], allowed to carefully establish the transcriptional pattern of core clock
336 regulators during the day. PERIOD genes *Per1*, *Per2* and *Cry2* display a maximum expression
337 level around noon, while *Cry1* expression peaks at sunset, in agreement with a PERIOD
338 complex-independent function of CRY1. Altogether this allows us to propose the following
339 model (Extended Data Fig. 6g): In the morning, the presence of the PERIOD complex (PER1/2
340 and CRY2) combined with the absence of CRY1, establishes an environment that favors HR
341 repair of TC-DSBs by allowing resection to occur, DSB anchoring to the NE and RAD51
342 loading. Subsequently, the gradual increase of CRY1 during the afternoon causes minimum
343 resection at night fall. The absence of PERIOD complex expression early at night establishes a
344 second layer of HR repression during the night. The gradual decrease of CRY1, combined with
345 the re-expression of PER proteins, then allows HR to resume the next morning.

346 **S**uch a tight regulation of HR at TC-DSBs during the night may be functionally relevant for
347 handling the repair of TC-DSBs produced in some specific contexts, such as in the brain
348 following neuronal activity[54,55]. Sleep was found to regulate the repair of DSBs in neurons[56].
349 Hence circadian regulation may fine-tune the response to this specific class of endogenous
350 DSBs.

351 In summary, our findings have implication for diseases etiology and treatment. Indeed,
352 evidence suggest that a dysregulation of the circadian clock contribute to the progression of
353 neurodegenerative disorders[57] and cancer initiation and progression[41,43], both types of diseases
354 being tightly coupled to DSB repair mechanisms and the maintenance of genome integrity.
355 Moreover, importantly, topoisomerase II poison-based chemotherapies are first-line treatment
356 against a number of cancers and given that these poisons mainly trigger DSBs in active
357 chromatin, our finding that circadian rhythm regulates the repair of TC-DSBs may be an
358 important feature to take into account for chronochemotherapy.

359

360

361

362 **Data and Code availability**

363 Code is available at https://github.com/LegubeDNAREPAIR/CircadianClock. High throughput
364 data are available at Array Express (E-MTAB-12712) using the link
365 https://www.ebi.ac.uk/biostudies/arrayexpress/studies/E-MTAB-12712?key=2f8af589-d077-
366 466a-a563-725b33761cda

367

368 **Acknowledgments**

369 We thank the genomics core facility of EMBL for high-throughput sequencing. We thank
370 Vanessa Dougados for her help during the RIM acquisitions and the LITC TRI-GENOTOUL
371 photonic imaging platform. We thank L. Ligat from the CRCT Cell Imaging Platform
372 (INSERM-UMR1037) for technical assistance in high-content microscopy. We thank T.
373 Clouaire and N. Firmin for technical help. We thank T. Clouaire, A. Marnef and E. Cau for

their advice throughout the project and critical reading of the manuscript. Development of 3D RIM on the LITC was supported by ANR-20-CE45-0024. Funding in GL laboratory was provided by grants from the European Research Council (ERC-2014-CoG 647344; and ERC-AdG-101019963), the Agence Nationale pour la Recherche (ANR-18-CE12-0015), the Association Contre le Cancer (ARC), the ITMO Cancer, the Ligue Nationale Contre le Cancer, comité de l'Aude and the Fondation Bettencourt-Schueller. C.A was a recipient of a FRM fellowship (FRM FDT201904007941), S.C. is a recipient of a PhD fellowship from the Joint Training and Research Programme on Chromatin Dynamics & the DNA Damage Response (H2020 ITN aDDRess, grant N° 812829). N.P is an INSERM researcher.

Authors contributions

B.L.B, L.G.S, E.G, C.P, C.A, A.G, A.L.F and N.P, performed and analyzed experiments. S.C and V.R performed bioinformatic analyses of all high-throughput sequencing datasets. T.M performed RIM acquisition and analysis. G.L. and N.P. supervised the work. G.L. wrote the manuscript. All authors commented, edited and approved the manuscript.

Conflict of interest

The authors declare no competing interest

References

1. Ballarino, R., Bouwman, B.A.M., Agostini, F., Harbers, L., Diekmann, C., Wernersson, E., Bienko, M., and Crosetto, N. (2022). An atlas of endogenous DNA double-strand breaks arising during human neural cell fate determination. Sci Data *9*, 400. 10.1038/s41597-022-01508-x.

2. Canela, A., Maman, Y., Huang, S.N., Wutz, G., Tang, W., Zagnoli-Vieira, G., Callen, E., Wong, N., Day, A., Peters, J.-M., et al. (2019). Topoisomerase II-Induced Chromosome Breakage and Translocation Is Determined by Chromosome Architecture and Transcriptional Activity. Molecular Cell *75*, 252-266.e8. 10.1016/j.molcel.2019.04.030.

402 3. Puget, N., Miller, K.M., and Legube, G. (2019). Non-canonical DNA/RNA structures during
403 Transcription-Coupled Double-Strand Break Repair: Roadblocks or Bona fide repair
404 intermediates? DNA Repair *81*, 102661. 10.1016/j.dnarep.2019.102661.

405 4. Brickner, J.R., Garzon, J.L., and Cimprich, K.A. (2022). Walking a tightrope: The complex balancing
406 act of R-loops in genome stability. Molecular Cell *82*, 2267–2297. 10.1016/j.molcel.2022.04.014.

407 5. Marnef, A., Cohen, S., and Legube, G. (2017). Transcription-Coupled DNA Double-Strand Break
408 Repair: Active Genes Need Special Care. Journal of Molecular Biology *429*, 1277–1288.
409 10.1016/j.jmb.2017.03.024.

410 6. Caron, P., van der Linden, J., and van Attikum, H. (2019). Bon voyage: A transcriptional journey
411 around DNA breaks. DNA Repair *82*, 102686. 10.1016/j.dnarep.2019.102686.

412 7. Chen, Z., and Tyler, J.K. (2022). The Chromatin Landscape Channels DNA Double-Strand Breaks to
413 Distinct Repair Pathways. Front. Cell Dev. Biol. *10*, 909696. 10.3389/fcell.2022.909696.

414 8. Aymard, F., Bugler, B., Schmidt, C.K., Guillou, E., Caron, P., Briois, S., Iacovoni, J.S., Daburon, V.,
415 Miller, K.M., Jackson, S.P., et al. (2014). Transcriptionally active chromatin recruits homologous
416 recombination at DNA double-strand breaks. Nat Struct Mol Biol *21*, 366–374.
417 10.1038/nsmb.2796.

418 9. Clouaire, T., and Legube, G. (2015). DNA double strand break repair pathway choice: a chromatin
419 based decision? Nucleus *6*, 107–113. 10.1080/19491034.2015.1010946.

420 10. Aymard, F., Aguirrebengoa, M., Guillou, E., Javierre, B.M., Bugler, B., Arnould, C., Rocher, V.,
421 Iacovoni, J.S., Biernacka, A., Skrzypczak, M., et al. (2017). Genome-wide mapping of long-range
422 contacts unveils clustering of DNA double-strand breaks at damaged active genes. Nat Struct Mol
423 Biol *24*, 353–361. 10.1038/nsmb.3387.

424 11. Wei, L., Nakajima, S., Böhm, S., Bernstein, K.A., Shen, Z., Tsang, M., Levine, A.S., and Lan, L.
425 (2015). DNA damage during the G0/G1 phase triggers RNA-templated, Cockayne syndrome B-
426 dependent homologous recombination. Proc. Natl. Acad. Sci. U.S.A. *112*.
427 10.1073/pnas.1507105112.

428 12. Arnould, C., Rocher, V., Bader, A.S., Lesage, E., Puget, N., Clouaire, T., Mourad, R., Noordermeer,
429 D., Bushell, M., and Legube, G. (2021). ATM-dependent formation of a novel chromatin
430 compartment regulates the Response to DNA Double Strand Breaks and the biogenesis of
431 translocations (Molecular Biology) 10.1101/2021.11.07.467654.

432 13. Marnef, A., Finoux, A.-L., Arnould, C., Guillou, E., Daburon, V., Rocher, V., Mangeat, T., Mangeot,
433 P.E., Ricci, E.P., and Legube, G. (2019). A cohesin/HUSH- and LINC-dependent pathway controls
434 ribosomal DNA double-strand break repair. Genes Dev. *33*, 1175–1190.
435 10.1101/gad.324012.119.

436 14. Nagai, S., Dubrana, K., Tsai-Pflugfelder, M., Davidson, M.B., Roberts, T.M., Brown, G.W., Varela,
437 E., Hediger, F., Gasser, S.M., and Krogan, N.J. (2008). Functional Targeting of DNA Damage to a
438 Nuclear Pore-Associated SUMO-Dependent Ubiquitin Ligase. Science *322*, 597–602.
439 10.1126/science.1162790.

440 15. Ryu, T., Spatola, B., Delabaere, L., Bowlin, K., Hopp, H., Kunitake, R., Karpen, G.H., and Chiolo, I.
441 (2015). Heterochromatic breaks move to the nuclear periphery to continue recombinational
442 repair. Nat Cell Biol *17*, 1401–1411. 10.1038/ncb3258.

443 16. Oza, P., Jaspersen, S.L., Miele, A., Dekker, J., and Peterson, C.L. (2009). Mechanisms that regulate
444 localization of a DNA double-strand break to the nuclear periphery. Genes Dev. *23*, 912–927.
445 10.1101/gad.1782209.

446 17. Horigome, C., Oma, Y., Konishi, T., Schmid, R., Marcomini, I., Hauer, M.H., Dion, V., Harata, M.,
447 and Gasser, S.M. (2014). SWR1 and INO80 Chromatin Remodelers Contribute to DNA Double-
448 Strand Break Perinuclear Anchorage Site Choice. Molecular Cell *55*, 626–639.
449 10.1016/j.molcel.2014.06.027.

450 18. Clouaire, T., Rocher, V., Lashgari, A., Arnould, C., Aguirrebengoa, M., Biernacka, A., Skrzypczak,
451 M., Aymard, F., Fongang, B., Dojer, N., et al. (2018). Comprehensive Mapping of Histone
452 Modifications at DNA Double-Strand Breaks Deciphers Repair Pathway Chromatin Signatures.
453 Molecular Cell *72*, 250-262.e6. 10.1016/j.molcel.2018.08.020.

454 19. Iacovoni, J.S., Caron, P., Lassadi, I., Nicolas, E., Massip, L., Trouche, D., and Legube, G. (2010).
455 High-resolution profiling of γH2AX around DNA double strand breaks in the mammalian genome.
456 EMBO J *29*, 1446–1457. 10.1038/emboj.2010.38.

457 20. Cohen, S., Puget, N., Lin, Y.-L., Clouaire, T., Aguirrebengoa, M., Rocher, V., Pasero, P., Canitrot, Y.,
458 and Legube, G. (2018). Senataxin resolves RNA:DNA hybrids forming at DNA double-strand
459 breaks to prevent translocations. Nat Commun *9*, 533. 10.1038/s41467-018-02894-w.

460 21. Cohen, S., Guenolé, A., Lazar, I., Marnef, A., Clouaire, T., Vernekar, D.V., Puget, N., Rocher, V.,
461 Arnould, C., Aguirrebengoa, M., et al. (2022). A POLD3/BLM dependent pathway handles DSBs in
462 transcribed chromatin upon excessive RNA:DNA hybrid accumulation. Nat Commun *13*, 2012.
463 10.1038/s41467-022-29629-2.

464 22. Zagelbaum, J., Schooley, A., Zhao, J., Schrank, B.R., Callen, E., Zha, S., Gottesman, M.E.,
465 Nussenzweig, A., Rabadan, R., Dekker, J., et al. (2022). Multiscale reorganization of the genome
466 following DNA damage facilitates chromosome translocations via nuclear actin polymerization.
467 Nat Struct Mol Biol. 10.1038/s41594-022-00893-6.

468 23. Brown, S.A., Ripperger, J., Kadener, S., Fleury-Olela, F., Vilbois, F., Rosbash, M., and Schibler, U.
469 (2005). PERIOD1-Associated Proteins Modulate the Negative Limb of the Mammalian Circadian
470 Oscillator. Science *308*, 693–696. 10.1126/science.1107373.

471 24. Duong, H.A., Robles, M.S., Knutti, D., and Weitz, C.J. (2011). A Molecular Mechanism for
472 Circadian Clock Negative Feedback. Science *332*, 1436–1439. 10.1126/science.1196766.

473 25. Padmanabhan, K., Robles, M.S., Westerling, T., and Weitz, C.J. (2012). Feedback Regulation of
474 Transcriptional Termination by the Mammalian Circadian Clock PERIOD Complex. Science *337*,
475 599–602. 10.1126/science.1221592.

476 26. Kim, J.Y., Kwak, P.B., and Weitz, C.J. (2014). Specificity in Circadian Clock Feedback from Targeted
477 Reconstitution of the NuRD Corepressor. Molecular Cell *56*, 738–748.
478 10.1016/j.molcel.2014.10.017.

479 27. Emerson, J.M., Bartholomai, B.M., Ringelberg, C.S., Baker, S.E., Loros, J.J., and Dunlap, J.C.
480 (2015). *period* -1 encodes an ATP-dependent RNA helicase that influences nutritional
481 compensation of the *Neurospora* circadian clock. Proc. Natl. Acad. Sci. U.S.A. *112*, 15707–15712.
482 10.1073/pnas.1521918112.

483 28. Ogilvie, V.C. (2003). The highly related DEAD box RNA helicases p68 and p72 exist as
484 heterodimers in cells. Nucleic Acids Research *31*, 1470–1480. 10.1093/nar/gkg236.

485 29. Takahashi, J.S. (2017). Transcriptional architecture of the mammalian circadian clock. Nat Rev
486 Genet *18*, 164–179. 10.1038/nrg.2016.150.

487 30. Qu, M., Qu, H., Jia, Z., and Kay, S.A. (2021). HNF4A defines tissue-specific circadian rhythms by
488 beaconing BMAL1::CLOCK chromatin binding and shaping the rhythmic chromatin landscape. Nat
489 Commun *12*, 6350. 10.1038/s41467-021-26567-3.

490 31. Koike, N., Yoo, S.-H., Huang, H.-C., Kumar, V., Lee, C., Kim, T.-K., and Takahashi, J.S. (2012).
491 Transcriptional Architecture and Chromatin Landscape of the Core Circadian Clock in Mammals.
492 Science *338*, 349–354. 10.1126/science.1226339.

493 32. Tartour, K., and Padmanabhan, K. (2022). The Clock Takes Shape—24 h Dynamics in Genome
494 Topology. Front. Cell Dev. Biol. *9*, 799971. 10.3389/fcell.2021.799971.

495 33. Xiao, Y., Yuan, Y., Jimenez, M., Soni, N., and Yadlapalli, S. (2021). Clock proteins regulate
496 spatiotemporal organization of clock genes to control circadian rhythms. Proc. Natl. Acad. Sci.
497 U.S.A. *118*, e2019756118. 10.1073/pnas.2019756118.

498 34. Swartz, R.K., Rodriguez, E.C., and King, M.C. (2014). A role for nuclear envelope–bridging
499 complexes in homology-directed repair. MBoC *25*, 2461–2471. 10.1091/mbc.e13-10-0569.

500 35. Caridi, C.P., D'Agostino, C., Ryu, T., Zapotoczny, G., Delabaere, L., Li, X., Khodaverdian, V.Y.,
501 Amaral, N., Lin, E., Rau, A.R., et al. (2018). Nuclear F-actin and myosins drive relocalization of
502 heterochromatic breaks. Nature *559*, 54–60. 10.1038/s41586-018-0242-8.

503 36. Mangeat, T., Labouesse, S., Allain, M., Negash, A., Martin, E., Guénolé, A., Poincloux, R., Estibal,
504 C., Bouissou, A., Cantaloube, S., et al. (2021). Super-resolved live-cell imaging using random
505 illumination microscopy. Cell Reports Methods *1*, 100009. 10.1016/j.crmeth.2021.100009.

506 37. Lottersberger, F., Karssemeijer, R.A., Dimitrova, N., and de Lange, T. (2015). 53BP1 and the LINC
507 Complex Promote Microtubule-Dependent DSB Mobility and DNA Repair. Cell *163*, 880–893.
508 10.1016/j.cell.2015.09.057.

509 38. Lieberman-Aiden, E., van Berkum, N.L., Williams, L., Imakaev, M., Ragoczy, T., Telling, A., Amit, I.,
510 Lajoie, B.R., Sabo, P.J., Dorschner, M.O., et al. (2009). Comprehensive Mapping of Long-Range
511 Interactions Reveals Folding Principles of the Human Genome. Science *326*, 289–293.
512 10.1126/science.1181369.

513 39. Falk, M., Feodorova, Y., Naumova, N., Imakaev, M., Lajoie, B.R., Leonhardt, H., Joffe, B., Dekker,
514 J., Fudenberg, G., Solovei, I., et al. (2019). Heterochromatin drives compartmentalization of
515 inverted and conventional nuclei. Nature *570*, 395–399. 10.1038/s41586-019-1275-3.

516 40. Roukos, V., Voss, T.C., Schmidt, C.K., Lee, S., Wangsa, D., and Misteli, T. (2013). Spatial Dynamics
517 of Chromosome Translocations in Living Cells. Science *341*, 660–664. 10.1126/science.1237150.

518 41. Sancar, A., and Van Gelder, R.N. (2021). Clocks, cancer, and chronochemotherapy. Science *371*,
519 eabb0738. 10.1126/science.abb0738.

520 42. Kondratov, R.V., and Antoch, M.P. (2007). Circadian proteins in the regulation of cell cycle and
521 genotoxic stress responses. Trends in Cell Biology *17*, 311–317. 10.1016/j.tcb.2007.07.001.

522 43. Masri, S., and Sassone-Corsi, P. (2018). The emerging link between cancer, metabolism, and
523 circadian rhythms. Nat Med *24*, 1795–1803. 10.1038/s41591-018-0271-8.

524 44. Mure, L.S., Le, H.D., Benegiamo, G., Chang, M.W., Rios, L., Jillani, N., Ngotho, M., Kariuki, T.,
525 Dkhissi-Benyahya, O., Cooper, H.M., et al. (2018). Diurnal transcriptome atlas of a primate across
526 major neural and peripheral tissues. Science *359*, eaao0318. 10.1126/science.aao0318.

527 45. Alexandrou, A.T., Duan, Y., Xu, S., Tepper, C., Fan, M., Tang, J., Berg, J., Basheer, W., Valicenti, T.,
528 Wilson, P.F., et al. (2022). PERIOD 2 regulates low-dose radioprotection via PER2/pGSK3β/β-
529 catenin/Per2 loop. iScience *25*, 105546. 10.1016/j.isci.2022.105546.

530 46. Papp, S.J., Huber, A.-L., Jordan, S.D., Kriebs, A., Nguyen, M., Moresco, J.J., Yates, J.R., and Lamia,
531 K.A. (2015). DNA damage shifts circadian clock time via Hausp-dependent Cry1 stabilization. eLife
532 *4*, e04883. 10.7554/eLife.04883.

533 47. Shafi, A.A., McNair, C.M., McCann, J.J., Alshalalfa, M., Shostak, A., Severson, T.M., Zhu, Y.,
534 Bergman, A., Gordon, N., Mandigo, A.C., et al. (2021). The circadian cryptochrome, CRY1, is a
535 pro-tumorigenic factor that rhythmically modulates DNA repair. Nat Commun *12*, 401.
536 10.1038/s41467-020-20513-5.

537 48. Anabtawi, N., Cvammen, W., and Kemp, M.G. (2021). Pharmacological inhibition of
538 cryptochrome and REV-ERB promotes DNA repair and cell cycle arrest in cisplatin-treated human
539 cells. Sci Rep *11*, 17997. 10.1038/s41598-021-97603-x.

540 49. Gaddameedhi, S., Selby, C.P., Kaufmann, W.K., Smart, R.C., and Sancar, A. (2011). Control of skin
541 cancer by the circadian rhythm. Proc. Natl. Acad. Sci. U.S.A. *108*, 18790–18795.
542 10.1073/pnas.1115249108.

543 50. Zhang, C., Chen, L., Sun, L., Jin, H., Ren, K., Liu, S., Qian, Y., Li, S., Li, F., Zhu, C., et al. (2023).
544 BMAL1 collaborates with CLOCK to directly promote DNA double-strand break repair and tumor
545 chemoresistance. Oncogene. 10.1038/s41388-023-02603-y.

546 51. Liu, Q., Pante, N., Misteli, T., Elsagga, M., Crisp, M., Hodzic, D., Burke, B., and Roux, K.J. (2007).
547 Functional association of Sun1 with nuclear pore complexes. Journal of Cell Biology *178*, 785–
548 798. 10.1083/jcb.200704108.

549 52. Li, P., and Noegel, A.A. (2015). Inner nuclear envelope protein SUN1 plays a prominent role in
550 mammalian mRNA export. Nucleic Acids Res, gkv1058. 10.1093/nar/gkv1058.

551 53. Talamanca, L., Gobet, C., and Naef, F. (2023). Sex-dimorphic and age-dependent organization of
552 24-hour gene expression rhythms in humans. Science *379*, 478–483. 10.1126/science.add0846.

553 54. Madabhushi, R., Gao, F., Pfenning, A.R., Pan, L., Yamakawa, S., Seo, J., Rueda, R., Phan, T.X.,
554 Yamakawa, H., Pao, P.-C., et al. (2015). Activity-Induced DNA Breaks Govern the Expression of
555 Neuronal Early-Response Genes. Cell *161*, 1592–1605. 10.1016/j.cell.2015.05.032.

556 55. Wei, P.-C., Chang, A.N., Kao, J., Du, Z., Meyers, R.M., Alt, F.W., and Schwer, B. (2016). Long
557 Neural Genes Harbor Recurrent DNA Break Clusters in Neural Stem/Progenitor Cells. Cell *164*,
558 644–655. 10.1016/j.cell.2015.12.039.

559 56. Zada, D., Sela, Y., Matosevich, N., Monsonego, A., Lerer-Goldshtein, T., Nir, Y., and Appelbaum, L.
560 (2021). Parp1 promotes sleep, which enhances DNA repair in neurons. Molecular Cell *81*, 4979-
561 4993.e7. 10.1016/j.molcel.2021.10.026.

562 57. Nassan, M., and Videnovic, A. (2022). Circadian rhythms in neurodegenerative disorders. Nat Rev
563 Neurol *18*, 7–24. 10.1038/s41582-021-00577-7.

564 58. Caron, P., Choudjaye, J., Clouaire, T., Bugler, B., Daburon, V., Aguirrebengoa, M., Mangeat, T.,
565 Iacovoni, J.S., Álvarez-Quilón, A., Cortés-Ledesma, F., et al. (2015). Non-redundant Functions of
566 ATM and DNA-PKcs in Response to DNA Double-Strand Breaks. Cell Reports *13*, 1598–1609.
567 10.1016/j.celrep.2015.10.024.

568 59. Zhou, Y., Caron, P., Legube, G., and Paull, T.T. (2014). Quantitation of DNA double-strand break
569 resection intermediates in human cells. Nucleic Acids Research *42*, e19–e19.
570 10.1093/nar/gkt1309.

571 60. Li, Q. (2004). A Syntaxin 1, G o, and N-Type Calcium Channel Complex at a Presynaptic Nerve
572 Terminal: Analysis by Quantitative Immunocolocalization. Journal of Neuroscience *24*, 4070–
573 4081. 10.1523/JNEUROSCI.0346-04.2004.

574 61. van Steensel, B., van Binnendijk, E.P., Hornsby, C.D., van der Voort, H.T., Krozowski, Z.S., de
575 Kloet, E.R., and van Driel, R. (1996). Partial colocalization of glucocorticoid and mineralocorticoid
576 receptors in discrete compartments in nuclei of rat hippocampus neurons. Journal of Cell Science
577 *109*, 787–792. 10.1242/jcs.109.4.787.

578 62. Arnould, C., Rocher, V., Finoux, A.-L., Clouaire, T., Li, K., Zhou, F., Caron, P., Mangeot, Philippe.E.,
579 Ricci, E.P., Mourad, R., et al. (2021). Loop extrusion as a mechanism for formation of DNA
580 damage repair foci. Nature *590*, 660–665. 10.1038/s41586-021-03193-z.

581

582 **Figure Legends**

583

584 **Figure 1: A multi-output screen for the identification of new TC-DSBR factors.**

585 **a**. Experimental scheme: DIvA cells allow to temporally induce, following treatment with 4-
586 hydroxytamoxifen (4-OHT), DSBs at annotated positions on the human genome, among which
587 >50% fall in active loci (TC-DSBs). TC-DSB potential interacting partners were identified
588 through a proteomic approach[13]. 130 proteins were further subjected to a multi output screen in
589 AID-DIvA cells using a siRNA library, to score γH2AX foci intensity, cell survival,
590 chromosome rearrangement and DSB clustering after DSB induction by 4-OHT. Data are
591 expressed normalized to the Control siRNA (CTRL, black). A positive control (SETX) was
592 included in the experiment (red bar). PPHLN1 and PER complex siRNAs are highlighted in
593 green and blue respectively.

594 **b**. γH2AX foci intensity was scored in siRNA transfected cells, using quantitative high
595 throughput imaging.

596 **c**. Cell survival of siRNA transfected cells was quantified eight days after DSB induction, using
597 a colorimetric assay based on mitochondrial dehydrogenase activity in viable cells.

598 **d**. DSB-induced rearrangement frequency *t(MIS12;TRIM37)* was analyzed by qPCR following
599 DSB induction and repair.

600 **e**. γH2AX foci mean area was scored in siRNA transfected cells, using quantitative high
601 throughput imaging.

602 **f-i**. Scatter plots showing the correlations for each siRNA between γH2AX intensity and cell
603 survival (**f**); γH2AX intensity and translocations (**g**); translocations and DSB clustering (**h**) and

604 cell survival and translocations (**i**). The 95% confidence intervals and the coefficient of
605 correlation (r, Pearson) are indicated.

606

607 **Figure 2. PER proteins regulate γH2AX foci formation, translocation, and cell survival**
608 **upon DSB induction**

609 **a**. γH2AX staining performed in control (CTRL), PER1 or PER2-siRNA transfected DIvA
610 cells, before (-DSB) and after (+DSB) DSB induction. Quantification is shown on the bottom
611 panel (>7000 nuclei, from a representative experiment). Center line: median; box limits: 1st
612 and 3rd quartiles; whiskers: maximum and minimum without outliers. *P*, unpaired t-test.

613 **b**. γH2AX ChIP performed in DIvA cells transfected with siRNA control (CTRL) or PER2
614 before and after DSB induction and analyzed by qPCR at two DSBs (DSB1-2). Data are
615 normalized to a control location devoid of a DSB. Mean and SEM are shown for n =4 biological
616 replicates. *P,* paired t-test (two-sided).

617 **c**. *t(MIS12:TRIM37)* rejoining frequencies after DSB induction measured by qPCR in AID-
618 DIvA cells transfected with siRNA CTRL, PER1 PER2, DDX17, SETX, NONO, DDX5 and
619 BMAL1. Mean and SD (n ≥4 biological replicates) are shown. *P*, paired t-test (two-sided).

620 **d**. Clonogenic assays in AID-DIvA cells transfected with siRNA CTRL, PER1, PER2, DDX17,
621 NONO, DDX5 or BMAL1. Left and right panels show the mean and SEM after 4-OHT
622 treatment (+DSB) and after IAA treatment (+DSB+Repair) respectively (n ≥4 biological
623 replicates). *P*, paired t-test (two-sided).

624

625 **Figure 3. PER2 is recruited at DSBs and promotes Homologous Recombination repair**

626 **a**. PER2, DDX5, DDX17 and BMAL1 ChIP efficiency (expressed as % of input
627 immunoprecipitated) before (−DSB) and after (+DSB) DSB induction, at a control genomic
628 locus devoid of DSB, a promoter (*BTG2* or *PER1* as indicated), and DSB1 or DSB-4. Mean
629 and SEM are shown for n ≥10 replicates. *P*, paired t-test (two-sided).

630 **b**. Genomic tracks showing RNA Polymerase II before DSB induction (RNAPII, green),
631 BLESS after DSB induction (black), as well as BMAL1 (blue) and PER2 (purple)
632 (log2(+DSB/−DSB)) at a TC-DSB (upper panel; chr21:460221789) and a DSB induced in a
633 silent locus (lower panel; chr12:130091880). DSBs are indicated by arrows.

634 **c**. Average PER2 (left) and BMAL1 (right) ChIP-seq profiles on a ±5 kb window centered on
635 the eighty best-induced AsiSI-DSBs (top) or eighty random sites (bottom, no DSB). Data are
636 presented in log2(+DSB/-DSB).

637 **d**. Box plots representing Log2 (+DSB/-DSB) PER2 ChIP-seq count on a ±2kb at HR-DSB,
638 NHEJ-DSB or random sites (30 in each category). Center line: median; box limits: 1st and 3rd
639 quartiles; whiskers: maximum and minimum without outliers. *P*-values, Wilcoxon test.

640 **e**. Resection assay. (Left) Schematic representation. (Right) quantification of single-strand
641 DNA in control, PER1, PER2 or CtIP siRNA-depleted DIvA cells at two distances (200bp and
642 1626bp as indicated) from the DSB-1 and at 1122bp from DSB-7. Mean and SEM are shown
643 for n ≥ 3 biologically independent experiments. *: $P<0.05$, **: $P<0.01$, ***: $P<0.001$, ns: not
644 significant. Paired t-test (two-sided)

645 **f**. RAD51 ChIP-qPCR in DIvA cells transfected with control or PER2 siRNA before and after
646 DSB induction, at four TC-DSBs (DSB1-4) and one DSB in a silent locus (DSB5). Data are
647 normalized to a control location devoid of a DSB, and further expressed relative to data obtained
648 at DSB4. Mean and SEM are shown for n=3 biological replicates. *P*, paired t-test (two-sided).

649 **g**. RT-qPCR performed before (−DSB) and after (+DSB) DSB induction in control (CTRL),
650 PER1 or PER2 siRNA-depleted DIvA cells for six genes carrying TC-DSB (relative to
651 untreated sample (-DSB)). Mean and SEM are shown for n=6 biological replicates. *P*, paired t-
652 test (two-sided).

653

654 **Figure 4: TC-DSBs are targeted to the nuclear envelope through the Sun-domain protein**
655 **SUN1**

656 **a**. Super-resolution Live imaging performed using Random Illumination microscopy (RIM) in
657 DIvA cells expressing 53BP1-GFP and mCherry-LaminB1, starting >1h after DSB induction.
658 Arrows show the establishment of a contact between a focus and nuclear lamina. Images were
659 acquired every 40s. Scale bar 1μM.

660 **b**. Proximity Ligation Assay (PLA) performed using either 53BP1 antibody (top panels),
661 Lamin B1 antibody (middle panels) or both 53BP1 and LaminB1 antibodies (bottom panels)
662 before (-DSB) and after DSB (+DSB) induction in DIvA cells. PLA quantification is shown on
663 the right panel. An average of 190 cells were analyzed per condition. Center line: median; box
664 limits: 1st and 3rd quartiles; whiskers: maximum and minimum without outliers. *P*, non-
665 parametric Wilcoxon test.

666 **c**. LaminB1 ChIP-qPCR before (−DSB) and after (+DSB) DSB induction, at TC-DSBs (HR-
667 DSBs, DSB1-4) and one DSB induced in a silent locus and repaired by NHEJ (DSB5). Data
668 are normalized to a control location devoid of a DSB. Mean and SEM are shown for n≥3
669 biological replicates. *P*, paired t-test (two-sided).

670 **d**. Genomic tracks of SUN1(purple) and SUN2 (dark blue) ChIP-seq (log2(+DSB/-DSB)) at a
671 TC-DSB (upper panel; chr17:57184296) and a DSB induced in a silent locus (lower panel;
672 chr12:130091880).

673 **e**. Average profiles of SUN1 (left) and SUN2 (right) on a ±5 kb window centered on the eighty
674 best-induced AsiSI-DSBs (top) or eighty random sites (bottom, no DSB). Data are presented as
675 log2(+DSB/-DSB).

676 **f**. γH2AX staining combined with SUN2 (top panel) or SUN1 (bottom panel) performed in
677 DIvA cells after DSB induction and acquired using 3D RIM Super-resolution microscope. The
678 areas represented in yellow (ICQ > 0.45) correspond to a high non-random colocalization (see
679 methods).

680 **g**. Left panels: Magnifications of SUN2 (top panels) and SUN1 (bottom panels) staining in
681 nuclear envelope (dotted line) together with γH2AX foci. Arrows indicate sites of
682 colocalization. Scale bar 1.5µM. Right panels: Cross Correlation Function (CCF) plots between
683 γH2AX foci and NE-embedded SUN2 (top panel, N=70 γH2AX foci) or SUN1 (bottom panel,
684 N=46 γH2AX foci). CCF of bicolor 3D RIM images was determined by plotting the value of
685 Pearson's correlation coefficient P[0.1] against Δx for each voxel of the image (see methods).
686 The arrows show a non-random exclusion between γH2AX and SUN2 (dip at Δx=0) or a non-
687 random overlap between the signals of SUN1and γH2AX (peak at Δx=0).

688 **h**. Clonogenic assays in AID-DIvA cells transfected with control (CTRL), SUN1 or SUN2-
689 siRNA. Mean and SEM after OHT treatment (+DSB) and after IAA treatment (+DSB+Repair)
690 are shown (n=5 biological replicates). *P*, paired t-test (two-sided). *: $P<0.05$, ns: not significant.

691 **i**. *t(MIS12:TRIM37)* and *t(LINC00271:LYRM2)* rejoining frequencies measured by qPCR in
692 AID-DIvA cells transfected with control (CTRL), SUN1 or SUN2-siRNA. Mean and SEM (n≥4
693 biological replicates) are shown. *P*, paired t-test (two-sided). *: $P<0.05$, **: $P<0.01$.

694

695 **Figure 5. PER proteins promote DSB nuclear envelope targeting and counteract DSB**
696 **clustering**

697 **a**. LaminB1 ChIPqPCR before (−DSB) and after (+DSB) DSB induction in control and PER2
698 siRNA-depleted DIvA cells, at TC-DSBs (DSB1-4, HR-DSBs) and a DSB in a silent locus
699 (DSB5, NHEJ-DSBs). Data are normalized to a control location devoid of DSB. Mean and
700 SEM are shown for n=4 biological replicates. *P*, paired t-test (two-sided).

701 **b**. Number of PLA foci (53BP1-LaminB1) in CTRL, PER1 or PER2-siRNA transfected DIvA
702 cells as indicated, before (−DSB) and after (+DSB) DSB induction. Data were normalized to
703 the untreated samples. Mean and SEM (n=3 biological replicates) are shown. *P*, paired t-test
704 (two-sided).

705 **c**. Number of PLA foci (γH2AX-LaminB1) following DSB induction in DIvA cells transfected
706 with CTRL or PER2 siRNA, in G1, S, and G2 cells determined by EdU and DAPI
707 incorporation. >7000 nuclei were acquired in each condition for each biological replicates. Data
708 were normalized to untreated cells (-DSB). Mean and SEM (n=3 biological replicates) are
709 shown. *P*-values, non-parametric Wilcoxon test.

710 **d**. Clonogenic assay in control, PER1, PER2, PER1+SUN1 and PER2+SUN1 siRNA
711 transfected AID-DIvA cells after DSB induction (+DSB, left panel), and after DSB induction
712 and IAA treatment allowing DSB repair (+DSB+repair, right panel). Mean and SEM are shown
713 for n=4 biologically independent experiments. *P*, paired t-test (two-sided).

714 **e**. Differential Hi-C contact matrix [(+DSB)-(-DSB)] on a region located on chromosome 2 at
715 25kb resolution in DIvA cells transfected with a control siRNA or a siRNA directed against
716 PER2 as indicated. γH2AX ChIP-seq track (+DSB) are also shown (red).

717 **f**. Interchromosomal DSBs interaction shown as aggregate peak analysis (APA) plotted on a
718 200kb window (10kb resolution) before (-DSB) and after DSB (+DSB) induction in control and
719 PER2 siRNA-transfected DIvA cells for the eighty best-induced AsiSI-DSBs (left) or eighty
720 random sites (right, no DSB). FC: Fold change calculated between the central pixel and a square
721 of 3x3 pixels on the bottom left corner of the matrix. APAs show an increased signal at the
722 center (DSB-DSB interaction) after DSBs induction only for DSB sites (FC= 3.49, compared
723 to 0.89 for random sites)). The signal increases after PER2 depletion (FC= 3.85).

724 **g**. Box plot showing the differential Hi-C read counts (as (log2 +DSB/-DSB)) between the 80
725 best induced DSBs (+/- 500kb) (left) or 80 random sites (right) in control (CTRL, grey) and
726 PER2 (purple) siRNA-transfected DIvA cells. Center line: median; box limits: 1st and 3rd
727 quartiles; whiskers: maximum and minimum without outliers. *P*, non-parametric Wilcoxon test.

728 **h**. Genomic tracks of γH2AX ChIP-seq after DSB induction(red) and of Chromosomal Eigen
729 vectors (CEV) obtained from PCA analyses performed on differential +DSB/-DSB Hi-C
730 matrices. CEV in siCTRL (grey) and siPER2 (blue). The D-compartment is represented as
731 positive values. siPER2 triggered the appearance of the D-compartment on the chromosome 2
732 normally devoid of D compartmentalization post-DSB induction in DIvA cells (areas
733 highlighted in light grey).

734

735 **Figure 6. The Circadian rhythm regulates TC-DSB targeting to nuclear envelope and**
736 **RAD51 loading**

737 **a**. γH2AX foci intensity, measured by high content microscopy, in DIvA cells after DSB
738 induction (+DSB 2h), in G1, S and G2 phases at different time points after dexamethasone
739 (Dex) treatment (synchronization of the circadian rhythm). Bars at the different time points are
740 colored according to the PER2 expression level (from highest in blue, to lowest in white). Data

741 were normalized to the average. Mean and SEM (n = 3 biological replicates, with >3000 nuclei
742 acquired per experiment) are shown.

743 **b**. γH2AX ChIP-qPCR performed in DIvA cells before (-DSB) and after DSB (+DSB)
744 induction at 28h and 40h after dexamethasone treatment (Dex) at three TC-DSBs (DSB1-3).
745 Data were normalized to a control location devoid of DSB and expressed relative to DSB4-28h.
746 Mean and SEM for n=5 biological replicates. *P,* paired t-test (two-sided).

747 **c**. RAD51 ChIP-qPCR performed in DIvA cells before (-DSB) and after DSB (+DSB) induction
748 at 28h and 40h after dexamethasone (Dex) treatment at four TC-DSBs (DSB1-4) and two
749 NHEJ-DSBs (DSB5-6). Data were normalized to a control location devoid of DSB and
750 expressed relative to DSB4-28h. Mean and SEM for n=6 biological replicates. *P*, paired t-test
751 (two-sided).

752 **d**. LaminB1 ChIP-qPCR performed in DIvA cells before (-DSB) and after DSB induction
753 (+DSB) at 28h and 40h after dexamethasone (Dex) treatment at four TC-DSBs (DSB1-4) and
754 DSB5 (DSB in silent locus). Data were normalized to a control location devoid of DSB and
755 expressed relative to the undamaged condition. Mean and SEM for n=5 biological replicates.
756 *P*, paired t-test (two-sided).

757 **e**. SUN1 ChIP-qPCR performed in DIvA cells before (-DSB) and after DSB induction (+DSB)
758 at 28h and 40h after dexamethasone (Dex) treatment at four TC-DSBs (DSB1-4) and DSB5.
759 Data are normalized to a control location devoid of DSB and further expressed related to data
760 obtained in the undamaged condition. Mean and SEM for n =3 biological replicates. *P*, paired
761 t-test (two-sided).

762 **f**. γH2AX foci mean area, measured by high content microscopy, in DIvA cells after DSB
763 induction (+DSB 2h), in G1, S and G2 phase at different time points after dexamethasone (Dex)

764 treatment. Data were normalized to the average. Mean and SEM (n=3 biological replicates) are
765 shown. *P*, paired t-test (two-sided).

766 **g**. DSB responsive genes expression was measured by RT-qPCR before (−DSB) and after
767 (+DSB) DSB induction in DIvA cells at 28h and 40h after dexamethasone treatment. cDNA
768 level of a D-compartment DSB responsive gene (*RNF19B*), two non-D compartment DSB
769 responsive genes (*PPM1D* and *SLC9A1*) and two control genes not regulated post DSB
770 induction (*LPHN2*, *UTP18*) are shown. Mean and SEM for n=4 biological replicates. *P,* paired
771 t-test (two-sided).

772 **h**. Model. During the day (PER phase), the PERIOD complex is recruited at DSBs occurring in
773 transcribed loci (TC-DSBs). This triggers the targeting of the TC-DSBs to the NE and their
774 tethering to the SUN1 INM protein, further ensuring RAD51 loading and HR repair. During
775 the night (BMAL1 phase), in absence of PER1/2, impaired TC-DSB anchoring to the NE leads
776 to impaired RAD51 loading, and enhanced DSB clustering and D-compartment formation.

777

778

779

780 **Methods**

781 **Cell culture and treatment**

782 U2OS, DIvA (AsiSI-ER-U20S)[19], AID-DIvA (AID-AsiSI-ER-U20S)[8] and 53BP1-GFP
783 DIvA[58] cells were grown in Dulbecco's modified Eagle's medium (DMEM) supplemented with
784 10%SVF (Invitrogen), antibiotics and either 1µg/mL puromycin (DIvA cells) or 800µg/mL
785 G418 (AID-DIvA cells) or both puromycin and G418 (53BP1-GFP DIvA) at 37°C under a
786 humidified atmosphere with 5%CO_2. The cell lines were regularly checked for mycoplasma
787 contamination. For AsiSI-dependent DSB induction, DIvA cell lines were treated with 300nM
788 4-hydroxytamoxifen (OHT) (Sigma, H7904) for 4h (unless otherwise indicated). For DSB
789 induction in U2OS, cells were treated with 1µM etoposide (Sigma, E1383) for 2h or with
790 10µg/mL Bleomycin (Sigma, B8416) for 2h. To stop inducing AsiSI-DSBs, AID-DIvA cells
791 were washed twice in pre-warmed PBS after OHT treatment and further incubated with 500µM
792 auxin (IAA) (Sigma, I5148) for 2h (unless otherwise indicated). For circadian rhythm
793 synchronization, cells were incubated for 1h with 500nM dexamethasone (Dex) Sigma,
794 D4902), then the medium was replaced (time = 0h). Dex treatment was done every 2h during
795 24h and the DSB induction was started for all synchronized cells at the same time, 24h after the
796 last Dex treatment, to obtain a full period circadian rhythm (analyses are shown from 24h to
797 46h post-Dex). To induce DSBs, synchronized cells are treated during 2h or 4h surrounding the
798 synchronization timepoint (*e.g.*, from 23h to 25h after Dex for a 2h treatment corresponding at
799 the synchronized time = 24h).

800

801 **Multi-output screen methodology**

802 Each of the 130 SMARTpool siRNAs from the TC-DSBR-focused siRNA library
803 (Extended Data Table 1) was transfected in 10^6 AID-DIvA cells as described below (siRNA
804 and plasmid transfection section), always including a negative (CTRL) and a positive (SETX)

805 control siRNAs. Transfected cells were plated (i) in 96-well Cell Carrier Ultra plates (20.000
806 cells/well in triplicates per condition) for γH2AX foci analysis (intensity and area) with
807 quantitative high throughput imaging as described below (High-Content microscopy and
808 Immunofluorescence sections); (ii) in 96-well plates (1000 cells/well in quadruplicates per
809 condition for cell survival analysis as described below (WST-1 cell survival assay section); and
810 in 10cm diameter dish for genomic DNA extraction and translocation frequency analysis as
811 described below (DSB-induced rearrangement /Translocation assay section). All data from
812 these different outputs post-DSB induction were expressed normalized to the negative control
813 siRNA (CTRL) and compared to the positive control siRNA (SETX).

814 **siRNA and plasmid transfection**

815 siRNA transfections were performed using the 4D-Nucleofector and the SE cell line
816 4D-Nucleofector X kit**s** (Lonza) according to the manufacturer's instructions. Briefly, 1-10µL
817 of 100µM annealed siRNA was transfected in 1-20x10^6 cells with 20-100µL SE solution in
818 Nucleocuvettes using the U2OS program CM-104. Subsequent cell treatments were performed
819 ~42-48h post-transfection. Most siRNAs used in this study were siGENOME SMARTpools
820 (Dharmacon) which are a mixture of 4 individual siRNAs, see Extended Data Table 1.
821 Individual siRNA sequences (Eurogentec) were used for SUN1, SUN2 or RBBP8/CtIP
822 (Extended Data Table 1). For all experiments, the control siRNA (CTRL) was the siGENOME
823 Non-Targeting Control siRNA Pool #2 (Dharmacon), except for Fig. 4h and Fig. 4i where the
824 control siRNA used with SUN1 and SUN2 siRNAs was Ctrl1 (Extended Data Table 1).

825 Plasmid transfections were performed using the 4D-Nucleofector and the SE cell line 4D-
826 Nucleofector X S kit (Lonza) according to the manufacturer's instructions. Briefly, 0.5µg DNA
827 was transfected in 10^6 cells with 20µL SE solution in Nucleocuvette strips using the U2OS
828 program CM-104, and subsequent OHT treatments were performed 48h later. mCherry-

829 LaminB1-10 plasmid was a gift from Michael Davidson (Addgene plasmid #55069;
830 http://n2t.net/addgene:55069 ; RRID:Addgene_55069).

831 **Immunofluorescence**

832 Transfected 53BP1-GFP DIvA cells were grown on glass coverslips and fixed with 4%
833 Paraformaldehyde during 15min at room temperature. After, 2 washes with PBS, the
834 permeabilization step was performed by treating cells with 0,5%Triton X-100 in PBS for
835 10min, then cells were blocked with PBS-BSA3% for 30min. Primary antibody against γH2AX
836 (Extended Data Table 4) was diluted in PBS-BSA3% and incubated with cells overnight at 4°C.
837 After 3 washes for 5min in PBS-BSA3%, cells were incubated with anti-mouse secondary
838 antibody (conjugated to Alexa594 or Alexa488, Invitrogen), diluted 1:1000 in PBS-BSA3%,
839 for 1h at room temperature. After a Hoechst 33342 (Invitrogen) staining (5µg/ml for 5min at
840 room temperature), Citifluor (AF1-25, Clinisciences) was used for coverslip mounting.

841 **High content microscopy (QIBC)**

842 U2OS, DIvA (AsiSI-ER-U20S)[19], AID-DIvA (AID-AsiSI-ER-Transfected or Dex-
843 synchronized DIvA and U20S cells were plated in 96-well Cell Carrier Ultra plates (Perkin
844 Elmer). Prior to the end of OHT, etoposide or bleomycin treatments, cells are treated with 10µM
845 EdU (Invitrogen, C10340) at 37 °C for 15min. For γH2AX staining, cells are fixed and
846 permeabilized as described above. For RAD51 staining, buffer II pre-extraction (20mM NaCl,
847 0.5% NP-40, 20mM HEPES at pH 7.5, 5mM $MgCl_2$, 1 mM DTT) was added to cells for 20min
848 on ice followed by fixation in 4% Paraformaldehyde during 15min at room temperature and
849 washed twice with PBS. Then EdU was labeled by Click-iT AlexaFluor 647 reaction
850 (Invitrogen, C10340) according to the manufacturer's instructions (cells protected from light
851 from now). Cells were washed twice for 5min in PBS-BSA3% and then blocked with PBS-
852 BSA3% for 30min at room temperature. Primary antibodies targeting γH2AX or RAD51

853 (Extended Data Table 4) were diluted in PBS-BSA3% and incubated with cells overnight at
854 4°C. After 3 washes of 3min in PBS-BSA3%, cells were incubated with anti-mouse Alexa 488
855 secondary antibody (Invitrogen) diluted 1:1000 in PBS-BSA3%, for 1h at room temperature.
856 After 3 washes of 3min in PBS, nuclei were labeled with 5µg/ml Hoechst 33342 (Invitrogen)
857 for 30min at room temperature. The cells were then washed twice with PBS and stored at 4°C.
858 γH2AX foci were further analyzed with an Operetta CLS High-Content Imaging System
859 (Perkin Elmer) and Harmony software (version 4.9). For quantitative image analysis, ~20-80
860 fields per well were acquired with a 20X (for γH2AX circadian synchronization) or 40X
861 objective lens to visualize >3000 cells per well in triplicate. Subsequent analyses were
862 performed with Columbus software (version 2.8.2). Briefly, the Hoechst-stained nuclei were
863 selected with B method, and the size and roundness of nuclei were used as parameters to
864 eliminate false positive compounds. Then, the Find Spots D method was used (Detection
865 sensitivity =0.2-0.4; Splitting coefficient =1; Background correction =0.5) to determine the
866 number, mean area and intensity of repair foci in each nucleus. For cell cycle analysis, the sum
867 of the Hoechst intensity and the mean of the EdU intensity were plotted in order to select G1,
868 S, and G2 cells.

869 **DSB- induced rearrangement/translocation assay**

870 AID-DIvA cells were treated as indicated and DNA was extracted using the DNeasy kit
871 (Qiagen). Illegitimate rejoining frequencies between different AsiSI sites, *t(MIS12;TRIM37)*
872 and *t(LINC00217;LYRM2)*, were analyzed by qPCR (in 3-4 replicates) using primers referenced
873 in Extended Data Table 3[20]. Results were normalized using two control regions (Norm1 and
874 Norm17) both far from any AsiSI sites and γH2AX domains (primers in Extended Data Table
875 3). Normalized translocation frequencies were calculated using the Bio-Rad CFX Manager 3.1
876 software.

877 **WST-1 cell survival assay**

878 Transfected AID-DIvA cells were plated in 96-well plates for each of the 3 conditions:
879 -DSB, +DSB, +DSB+repair. 48h later, cells were treated or not with OHT for 4h and further
880 incubated or not with IAA for 4h. Eight days after DSB induction, the medium is replaced by a
881 mix of 100µl warmed medium + 10µl WST-1 ready-to-use solution per well and the cells were
882 incubated for 2h at 37°C. The tetrazolium salts from Premix WST-1 Cell Proliferation Assay
883 System (TAKARA) are cleaved by mitochondrial dehydrogenase in viable cells to produce
884 formazan dye, which is quantified by measuring its absorbance at 450nm (Multiskan GO
885 Microplate Spectrophotometer from Thermo Fisher Scientific). The percentage of viable cells
886 is normalized to the undamaged cells and compared to the control condition.

887 **Clonogenic assays**

888 Transfected AID-DIvA cells were seeded, in duplicate, at a clonal density in 10cm
889 diameter dishes and, 48h later, were treated or not with 4OHT for 4h and washed twice in pre-
890 warmed PBS and further incubated with auxin (IAA) for another 4h when indicated. Then, the
891 medium was replaced for all cell dishes. After 8 days at 37°C under a humidified atmosphere
892 with 5%CO_2, cells were washed in PBS and stained with crystal violet (Sigma, V5265). Images
893 of stained colonies were obtained using the White Sample Tray for the ChemiDoc Touch
894 Imaging System (Bio-Rad) and colonies were counted using the Spot Detector plugin of Icy
895 software, Version 2.0.2.0 (icy.exe program). Only colonies containing more than 50 cells were
896 scored.

897

898 **Western blots**

899 DIvA cells were incubated in RIPA buffer (50mM Tris pH8.0, 150mM NaCl, 0.5%
900 sodium deoxycholate, 1% NP-40, 0.1% SDS) on ice for 20 min. Samples were further incubated

901 with 250 units of Benzonase (Sigma, E1014) per million of cells for 10 min at room
902 temperature, then centrifuged at 13,000 rpm for 10 min at 4°C. The supernatants, containing
903 soluble protein extracts, were then mixed with SDS loading buffer and reducing agent, and
904 incubated 10 min at 70°C. Electrophoreses were performed using 4–12% NuPAGE Bis-Tris
905 gels (Invitrogen) and semi-dry western blotting on nitrocellulose membranes (Bio-Rad) was
906 done with the Trans-Blot Turbo System (Bio-Rad) according to the manufacturer's instructions.
907 Membranes were incubated in TBS containing 0.1% Tween 20 (Sigma, P1379) and 4% BSA
908 during 1h at room temperature for blocking, followed by overnight incubation at 4 °C using
909 primary antibody diluted in TBS-Tween-4% BSA. The corresponding mouse or rabbit
910 horseradish peroxidase-coupled secondary antibodies (Sigma, A2554 and A0545) were used at
911 1:10,000 to reveal the proteins, using a luminol-based enhanced chemiluminescence HRP
912 substrate (Super Signal West Dura Extended Duration Substrate, ThermoScientific). Picture
913 acquisition of the membranes was done using the ChemiDoc Touch Imaging System (Bio-Rad)
914 and pictures were analyzed using Image Lab software (Bio-Rad). All primary antibodies used
915 in this study are detailed in Extended Data Table 4. Note: although different conditions and
916 several human PER1 antibodies were tested, none of them resulted in a ~140kDa signal
917 corresponding to the PER1 protein on the western-blots.

918 **RT-qPCR**

919 Total RNA was extracted from U2OS and DIvA cell lines before and after DSB
920 induction using homogenization with QIAshredder and the RNeasy kit (Qiagen) following the
921 manufacturer's instructions. RNA was then reverse transcribed to cDNA using the AMV
922 reverse transcriptase (Promega, M510F). qPCR experiments were performed to assess the
923 levels of cDNA using primers referenced in Extended Data Table 3. cDNA levels were then
924 normalized with GAPDH (Gene ID: 2597), TBP (Gene ID: 6908) and 18S (RNA18SN5, Gene
925 ID: 100008588) cDNA levels using the CFX Manager 3.1 software (Bio-Rad).

926 **Resection assay**

927 Measure of resection was performed as described in[59] with the following modifications.
928 Genomic DNA was extracted from transfected DIvA cells just after DSB induction using the
929 DNeasy kit (Qiagen) without any vortexing step. 1 µg of DNA was incubated 20min at 37°C
930 with 15 units of RNAseH1 (New England Biolabs) and first digested for 2h at 37°C with 35
931 units of AsiSI restriction enzyme (New England Biolabs). Then, 250ng of DNA were further
932 digested overnight at 37°C using 10 units of BanI restriction enzyme, that cuts at 200bp and
933 1626bp from the DSB1, or of BanII restriction enzyme, that cuts at 1122bp from the DSB7
934 (Extended Data Table 2). Both enzymes were heat inactivated for 20 min at 80°C. Digested and
935 undigested samples were analyzed by qPCR (10ng/well) using primers in Extended Data Table
936 3. ssDNA% was calculated with the following equation: Percent of ssDNA=
937 1/((PUISSANCE(2;(Ct Digested − Ct Non Digested) − 1) + 0.5))*100.

938 **Proximity Ligation Assay (PLA)**

939 PLA experiments were performed using Duolink® In Situ Detection assay from Sigma-
940 Aldrich according to the manufacturer's instructions. Primary antibodies used for PLA are
941 detailed in Extended Data Table 4.

942 ***γH2AX-LaminB1 PLA.*** siRNA-transfected or Dexamethasone-synchronized DIvA cells were
943 plated in 96-well Cell Carrier Ultra plates (Perkin Elmer). At the end of 4OHT treatment, cells
944 are treated with 10µM EdU (Invitrogen, C10340) for 15min. Cells are fixed with 4%
945 paraformaldehyde during 15min at room temperature. Permeabilization step was performed by
946 treating cells with 0,5% Triton X-100 in PBS for 5min. Then EdU was labeled by Click-iT
947 Alexa488 reaction (Invitrogen, C10340) according to the manufacturer's instructions. Cells
948 were blocked with 1 drop of blocking solution provided with the Duolink® PLA Probes
949 (DUO92002 and DUO92004, Sigma-Aldrich) for 1h at 37°C in a humid chamber. Primary

950 antibodies targeting γH2AX and LaminB1 were diluted in the antibody dilution buffer provided
951 with the Duolink® PLA Probes and incubated with cells overnight at 4°C. After two 5min
952 washes in Duolink® In Situ Wash Buffer A (DUO82049, sigma-Aldrich), cells were incubated
953 with anti-mouse plus and anti-rabbit minus probes for 1h at 37°C, under slow rotation. After
954 two washes in wash buffer A for 5min, cells were incubated for 30min at 37°C in the ligation
955 reaction mix from the Duolink® In Situ Detection Reagents Red (DUO92008, Sigma-Aldrich).
956 The cells were washed again twice in wash buffer A for 5min and incubated for 1h40 at 37°C
957 under slow rotation for the amplification step. Finally, after two 10min washes in wash buffer
958 B (DUO82049, sigma-Aldrich), nuclei were stained in the staining solution from the Duolink®
959 In Situ Microplate Nuclear Stain (DUO82064, Sigma-Aldrich) for 30min at 37°C and cells were
960 kept in the Anti-Fade solution (DUO82064, Sigma-Aldrich) until image acquisition. For
961 quantitative image analysis, images were acquired with a 40X objective lens to visualize >3000
962 cells per well in duplicate. Subsequent analyses were performed with Columbus software
963 (version 2.8.2) to determine the numbers of PLA foci in each nucleus. G1, S and G2 nuclei
964 were selected based on EdU and DAPI staining distribution in all cells.

965 ***53BP1-LaminB1 PLA.*** siRNA-transfected cells were seeded on 13mm coverslips and treated
966 for 4h with 4OHT before fixation in 4%PFA. Slides were then processed as before, except that
967 there were no EdU staining, and that at the end of the PLA procedure, after the two 10min
968 washes in wash buffer B, cells were then washed for 1min in 0.01% wash buffer B and mounted
969 on slides with Duolink® In Situ Mounting Medium with DAPI (DUO82040, Sigma-Aldrich).
970 Image acquisition was done on Leica DM6000 at 40X objective lens to visualize >175 cells per
971 experiment in triplicate. Subsequent analyses were performed with Cell Profiler software
972 (version 4.2.4) to determine the numbers of PLA foci in each nucleus.

973 **3D super resolution using Random Illumination Microscopy (RIM)**

974 ***3D RIM two cameras setup.*** The 3D RIM home-made setup is coupled to an inverted
975 microscope (TEi Nikon) equipped with 100x magnification, a 1.49 N.A. objective (CFI SR
976 APO 100XH ON 1.49 NIKON) and two SCMOS cameras (ORCA-Fusion, Hamamatsu)
977 mounted in an industrial apochromatic alignment module (abbelight SA). Fast diode lasers
978 (Oxxius) with wavelengths centered at 488nm (LBX-488-200-CSB) and 561nm (LMX-561L-
979 200-COL) are used for all experiments. The bandpass emission filters in front of the two
980 respective cameras are FF01-514/30-25 for camera 1 and FF01-609/54-25 for camera 2. The
981 binary phase modulator (QXGA fourth dimension) conjugated to the image plane combined
982 with polarization elements are used to generate dynamic speckle on the object plane as
983 described in[36]. The synchronization of the hardware (Z-platform, cameras, microscope, laser
984 and SLM) is performed by an improved version of the commercial software INSCOPER.

985 ***Fixed 3D RIM acquisition and reconstruction.*** Two-color 3D RIM imaging was
986 performed with the 3D RIM system. The acquisition of 40 planes was done sequentially with a
987 120nm step in the image plane. For each image plane, 400 speckles were used to increase the
988 desired super-resolved 3D resolution (95nm,95nm,200nm). The image reconstructions were
989 performed with the software (ALgoRIMhttps://github.com/teamRIM/tutoRIM). The Wiener
990 filter used is 0.01, the deconvolution parameter is 0.02 and the regularization parameter is 0.02
991 for the first channel images. The Wiener filter used is 0.02, the deconvolution parameter is 0.03
992 and the regularization parameter is 0.02 for the second channel images. The misalignment
993 between the two cameras and the residual chromatic aberrations are corrected using the SVI
994 (Scientific Volume Imaging) software.

995 ***3D+t two colors RIM super-resolution acquisition and reconstruction***. 3D+t RIM
996 movies were performed on AID-DIvA cells expressing 53BP1-GFP and mcherry-LaminB1. 3D
997 movies of 47min with 40sec intervals were made (60 times). The whole cell acquisition time

was 6 seconds with 48 random patterns optimized for live cells for each plane. Image reconstructions were performed with the software (ALgoRIMhttps://github.com/teamRIM/tutoRIM). The Wiener filter used is 0.01, the deconvolution parameter is 0.151 and the regularization parameter is 0.08 for the first channel images. The Wiener filter used is 0.1, the deconvolution parameter is 0.25 and the regularization parameter is 0.08 for the second channel images. The misalignment between the two cameras and the residual chromatic aberrations are corrected using the SVI (Scientific Volume Imaging) software.

3D film editing. Bleaching correction is performed after RIM reconstruction with the open-source FIJI 546 software (https://imagej.net/software/fiji/) based on an exponential FIT from the background. The FIJI 3D drift correction plugin is performed for 3D registration (https://github.com/fiji/Correct_3D_Drift). Rendering of 3D+t movies was performed with the VTK library implemented in ICY software (https://icy.bioimageanalysis.org/) from 3D CROP on 550 areas of interest. Chromatism correction was performed by Scientific Volume Imaging (SVI) software.

Colocalization analyses. The colocalization analyzer from the Scientific Volume Imaging (SVI) software is used on fixed 3D RIM images to quantify the interactions of γH2AX nanofoci with those of SUN1 and SUN2.

Quantitative immunocolocalization (ICQ). The intensity correlation quotient was defined in[60] by the following equation for each voxel "i":

$$\left(I_i^{D1} - I_{avg}^{D1}\right)\left(I_i^{D2} - I_{avg}^{D2}\right)$$

For a random or mixed interaction, this number will tend towards 0, and for a dependent correlation, it will tend towards +0.5. This parameter does not directly use the intensity of each

1021 pair of voxels and has the advantage of eliminating the bias towards particularly high or too
1022 low intensities.

1023 ***Cross-correlation function CCF.*** The Van Steensel cross-correlation function (VSCF) CCF is
1024 used to quantify interactions and has been described in[61]. It is obtained by calculating the
1025 Pearson coefficient after shifting the second camera image over a distance of Δx voxels.
1026 Thresholding was carefully tailored for each image to reject the 10th percentile of the lowest
1027 intensity value for both channels. The CCF was measured with the x-shift set to 940nm without
1028 rotation and the resulting three graphs were averaged and plotted with a 95 percentil. The
1029 Pearson coefficient is the classic equation below for each voxel "i":

1030
$$P = \frac{\sum\left(I_i^{D1} - I_{avg}^{D1}\right)\left(I_i^{D2} - I_{avg}^{D2}\right)}{\sqrt{\sum\left(I_i^{D1} - I_{avg}^{D1}\right)\left(I_i^{D2} - I_{avg}^{D2}\right)}}$$

1031 with I_{avg}^{D1} and I_{avg}^{D2} the averages of camera 1 and camera 2 of the microscope.

1032 For better visualization of the shape of the CCF function for each condition, we normalized the
1033 CCF function between 0 and 1 with the following normalization calculation:

1034
$$P_{(0,1)} = \frac{(P - P_{min})}{(P_{max} - P_{min})}$$

1035 Negative values for Δx indicate a shift in nm of the red image to the left, positive values indicate
1036 a shift to the right. Non-random overlap results in a peak at Δx=0 and non-random exclusion
1037 results in a dip at Δx=0. Uncorrelated distributions will not show any clear peak in the CCF.

1038 **ChIP-qPCR, ChIP-seq and data analysis**

1039 ***ChIP-qPCR.*** ChIP experiments were performed in DIvA cells according to the protocol
1040 described in[8,19] with 200µg of chromatin per immunoprecipitation. The quantity of primary
1041 antibodies used is detailed in Extended Data Table 4. qPCR experiments were performed on
1042 both IP and input samples to assess the percent of input DNA immunoprecipitated, using AsiSI-
1043 induced DSBs referenced in Extended Data Table 2 and primers detailed in Extended Data
1044 Table 3. When indicated in the figure legends, data are normalized to a control location devoid
1045 of DSB (Ctrl genomic locus) and could be further expressed related to data obtained at DSB4
1046 or in undamaged condition.

1047 ***Library preparation and sequencing.*** Multiple ChIP experiment samples were pooled and
1048 sonicated for 15 cycles (30 sec on, 30 sec off, high setting) with a Bioruptor (Diagenode), then
1049 concentrated with a vacuum (Eppendorf). 10ng of purified DNA (average size 250–300bp) was
1050 used to prepare sequencing libraries with the Next Ultra II Library Prep Kit for Illumina (New
1051 England Biolabs) using the application note for "Low input ChIP-seq", and subjected to 75bp
1052 single-end sequencing using Illumina NextSeq500 at the EMBL Genomics core facility
1053 (Heidelberg, Germany).

1054 ***ChIP-seq data processing***. ChIP-seq data processing was performed as described[18]. In brief,
1055 raw sequencing reads were aligned using bwa (https://bio-bwa.sourceforge.net/) to the human
1056 reference genome (hg19) and then, were sorted, deduplicated, and indexed using samtools
1057 (http://www.htslib.org/). Bigwig coverage tracks were subsequently extracted from the
1058 processed bam files using bamCoverage from deepTools (HYPERLINK
1059 https://deeptools.readthedocs.io/en/develop/), and were normalized by total read count to be
1060 used for downstream analyses.

1061 ***DSB Average profiles and boxplots.*** Differential coverage tracks representing the log2 ratio
1062 between damaged and undamaged ChIP-seq samples were created using the bamCompare

1063 function of deepTools on default settings. These bigwigs were then used as input for the
1064 computeMatrix function of deepTools to calculate the coverage at DSBs using 200 bins
1065 covering either 10kb or 1kb as indicated on Figures. These matrices were then processed using
1066 a custom script in R with ggplot2.

1067 ***Peak calling.*** Peak calling for ChIP-seq datasets (BMAL1, SUN1 and SUN2) was performed
1068 using *MACS2* using -q 0.1 for BMAL1 resulting in 1776 peaks, and -q 0.005 for SUN1 and
1069 SUN2 resulting in 27326 and 14571 peaks respectively.

1070 ***Gene Ontology Analysis.*** Genes for BMAL1 GO analysis were selected if the identified
1071 BMAL1 peak was within a genes body or within its promoter region. The subsequent gene list
1072 was used to perform gene ontology analysis using the *enrichGO* function
1073 from *clusterprofiler* in R.

1074 ***Peak annotation.*** The genomic locations of SUN1 and SUN2 peaks were identified by using
1075 the *ChIPseeker* package in R, specifically the *annotatePeak* function to annotate the regions
1076 and *plotAnnoPie* for subsequent visualization. To calculate the coverage of SUN1 at SUN2
1077 regions, the *computeMatrix* function of deepTools was used using 200 bins over a 10kb
1078 window. The matrix was then processed using a custom script in R with ggplot2.

1079 **Hi-C and data analyses**

1080 ***Hi-C libraries.*** Hi-C experiments were performed in DIvA cells following transfection with
1081 CTRL or PER2 siRNAs and with or without DSB induction as described in[62]. Briefly, 10^6 cells
1082 were used per condition. Hi-C libraries were generated using the Arima-HiC+ for HiC (Arima
1083 Genomics) by following the manufacturer's instructions. DNA was sheared using the Covaris
1084 S220 to obtain an average fragment size of 350-400pb. Sequencing libraries were prepared on
1085 beads using the Next Ultra II DNA Library Prep Kit for Illumina and Next Multiplex Oligos

1086 for Illumina (New England Biolabs) following instructions from the Arima-HiC+ for HiC
1087 (Arima Genomics). Hi-C data were processed as described in [12,62]see below.

1088 ***Hi-C heatmaps.*** Hi-C reads were mapped to hg19 and processed with Juicer v2.0 using default
1089 settings (https://github.com/aidenlab/juicer). Hi-C count matrices were generated using Juicer
1090 at multiple resolutions: 100kb, 50kb, 25kb, 10kb, 5kb and 1kb. Hi-C heatmap screenshots were
1091 obtained using Juicebox (https://github.com/aidenlab/Juicebox/wiki/Download).

1092 ***Aggregate Peak Analysis (APA).*** APA plots of inter- or intra-chromosomal interactions of
1093 DSBs and control regions were created using the APA program of Juicer tools (https://github.
1094 com/aidenlab/juicer/wiki/APA) with a 10kb resolution -/+ 100kb.

1095 ***Trans contact quantification.*** To determine inter-chromosomal interaction changes (in *trans*),
1096 we built the whole-genome Hi-C matrix for each experiment by merging all chromosome-
1097 chromosome interaction matrices using Juicer and R to obtain a genome matrix with 33kx33k
1098 bin interactions for 100kb resolution. Interactions between bins inside damaged TADs
1099 (240X240 for the 80 best-induced AsiSI DSBs) were extracted and counted for each condition,
1100 then log2 ratio was calculated on normalized count (cpm), and plotted as boxplots or heatmaps
1101 (https://github.com/LegubeDNAREPAIR/ATMcompD/blob/main/scriptR/Heatmap_D_trans.
1102 R).

1103 ***A/B compartment.*** To identify A and B main chromosomal compartments, the extraction of the
1104 first Eigen vector of the correlation matrix (PC1) was done on the Observed/Expected matrix
1105 at 500kb resolution using juicer eigenvector command. The resulting values were then
1106 correlated with ATAC-seq signal in order to attributes positive and negative values to the A
1107 and B compartment, respectively, on each chromosome. The Observed/Expected bins were then
1108 arranged based on the PC1 values and aggregated into 21 percentiles, to visualize A-B

1109 interactions on the siPER2 and siCTRL experiments (saddle plots), and differences were
1110 computed between PER2 and control conditions for each percentile.

1111 ***D-compartment.*** For D-compartment identification, we retrieved the first component (PC1) of
1112 a PCA made on the differential observed over expected Hi-C matrix $log2\left(\frac{damaged}{undamaged}\right)$ at 100kb
1113 resolution. Each matrix was extracted from the .hic files using Juicer and the ratio was
1114 computed bin per bin. Pearson Correlation matrices were then computed for each chromosome,
1115 and PCA was applied to each matrix. The first component of each PCA was then extracted and
1116 correlated with the position of DSBs. A PC1 showing a positive correlation with DSBs was
1117 then called D-compartment, and PC1 showing negative correlation with DSBs were multiplied
1118 by -1. We were able to extract the D-compartment on several chromosomes for +DSB/-DSB[12].
1119 D-compartment (first component of the PCA) was converted into a coverage file using
1120 rtracklayer R package. For analysis of DSB responsive gene expression by RT-qPCR, we used
1121 the previously determined D compartment genes as described in[12].

1122 **Contact for Reagent and Resource Sharing**

1123 Further requests for reagents and resources should be asked to the lab PI, Gaëlle Legube
1124 (gaelle.legube@univ-tlse3.fr). DIvA cell lines are subjected to an MTA with the CNRS.

1125

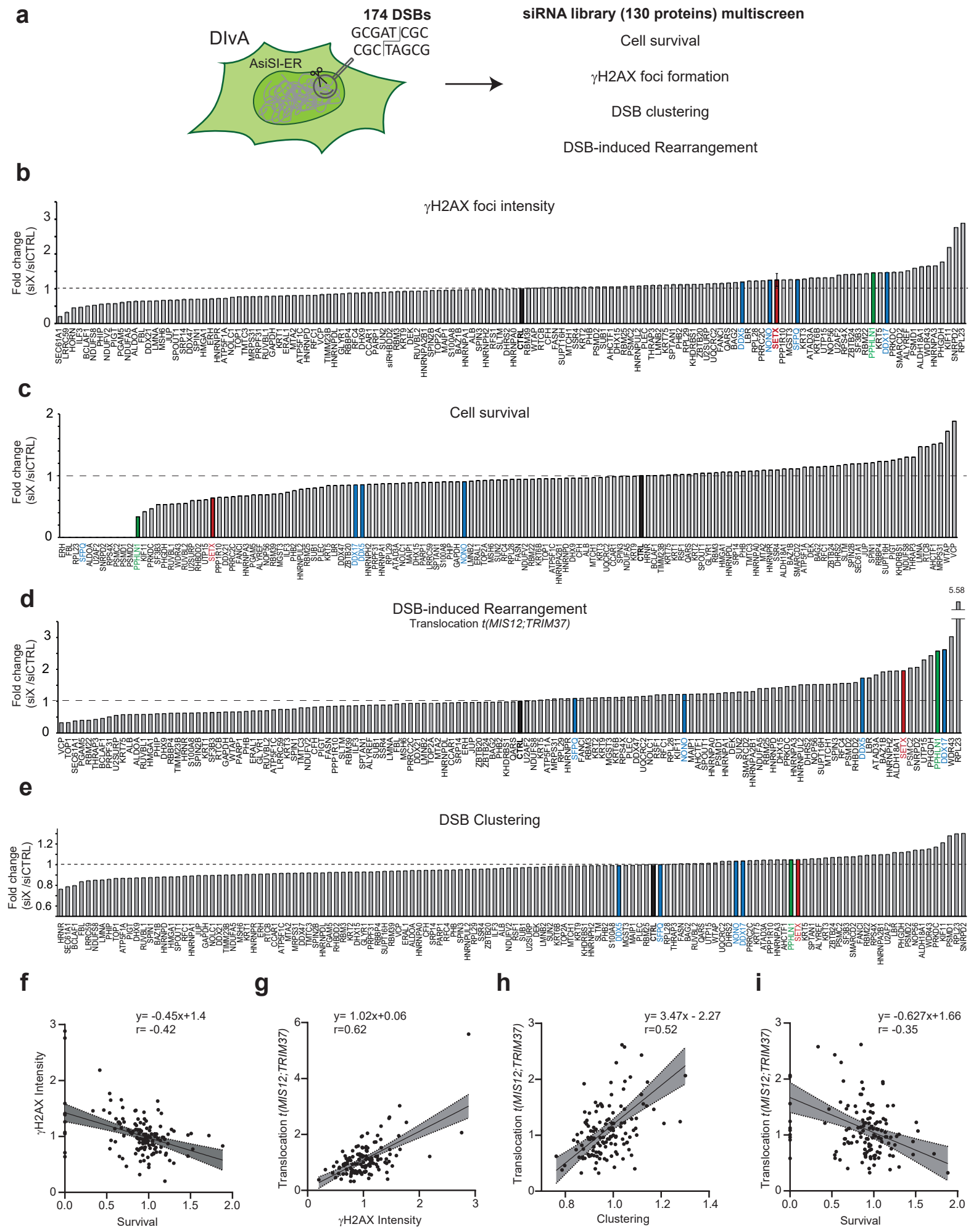
a
DIvA
AsiSI-ER
174 DSBs
GCGAT CGC
CGC TAGCG
siRNA library (130 proteins) multiscreen
Cell survival
γH2AX foci formation
DSB clustering
DSB-induced Rearrangement
b
γH2AX foci intensity
Fold change (siX /siCTRL)
c
Cell survival
Fold change (siX /siCTRL)
d
DSB-induced Rearrangement
Translocation t(MIS12;TRIM37)
5.58
Fold change (siX /siCTRL)
e
DSB Clustering
Fold change (siX /siCTRL)
f
y= -0.45x+1.4
r= -0.42
γH2AX Intensity
Survival
g
y= 1.02x+0.06
r=0.62
Translocation t(MIS12;TRIM37)
γH2AX Intensity
h
y= 3.47x - 2.27
r=0.52
Translocation t(MIS12;TRIM37)
Clustering
i
y= -0.627x+1.66
r= -0.35
Translocation t(MIS12;TRIM37)
Survival

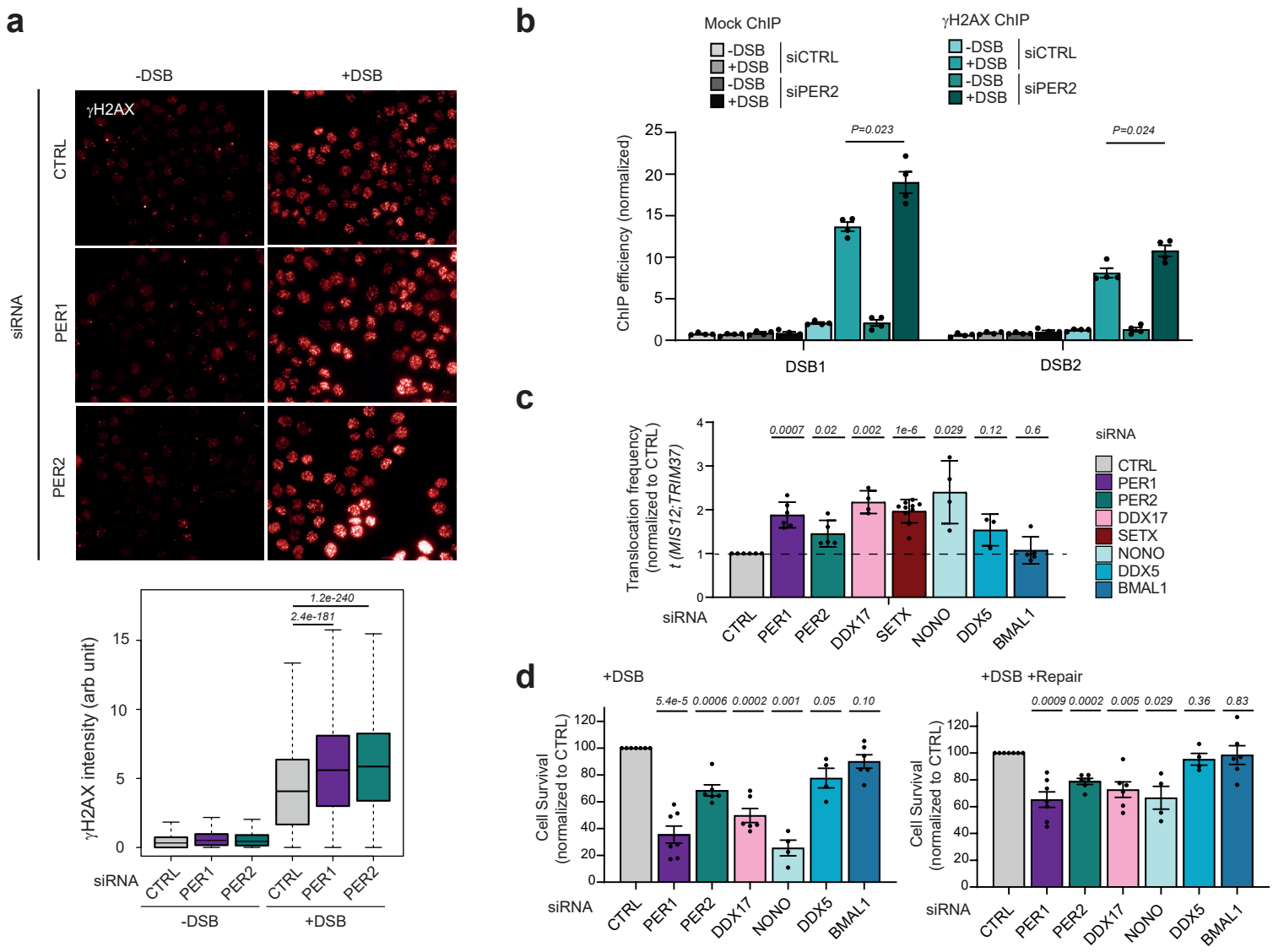
a
-DSB
+DSB
γH2AX
siRNA
CTRL
PER1
PER2
γH2AX intensity (arb unit)
1.2e-240
2.4e-181
siRNA
CTRL
PER1
PER2
CTRL
PER1
PER2
-DSB
+DSB
b
Mock ChIP
-DSB
+DSB
-DSB
+DSB
siCTRL
siPER2
γH2AX ChIP
-DSB
+DSB
-DSB
+DSB
siCTRL
siPER2
ChIP efficiency (normalized)
P=0.023
P=0.024
DSB1
DSB2
c
Translocation frequency (normalized to CTRL)
t (MIS12;TRIM37)
0.0007
0.02
0.002
1e-6
0.029
0.12
0.6
siRNA
CTRL
PER1
PER2
DDX17
SETX
NONO
DDX5
BMAL1
siRNA
CTRL
PER1
PER2
DDX17
SETX
NONO
DDX5
BMAL1
d
+DSB
Cell Survival (normalized to CTRL)
5.4e-5
0.0006
0.0002
0.001
0.05
0.10
siRNA
CTRL
PER1
PER2
DDX17
NONO
DDX5
BMAL1
+DSB +Repair
Cell Survival (normalized to CTRL)
0.0009
0.0002
0.005
0.029
0.36
0.83
siRNA
CTRL
PER1
PER2
DDX17
NONO
DDX5
BMAL1

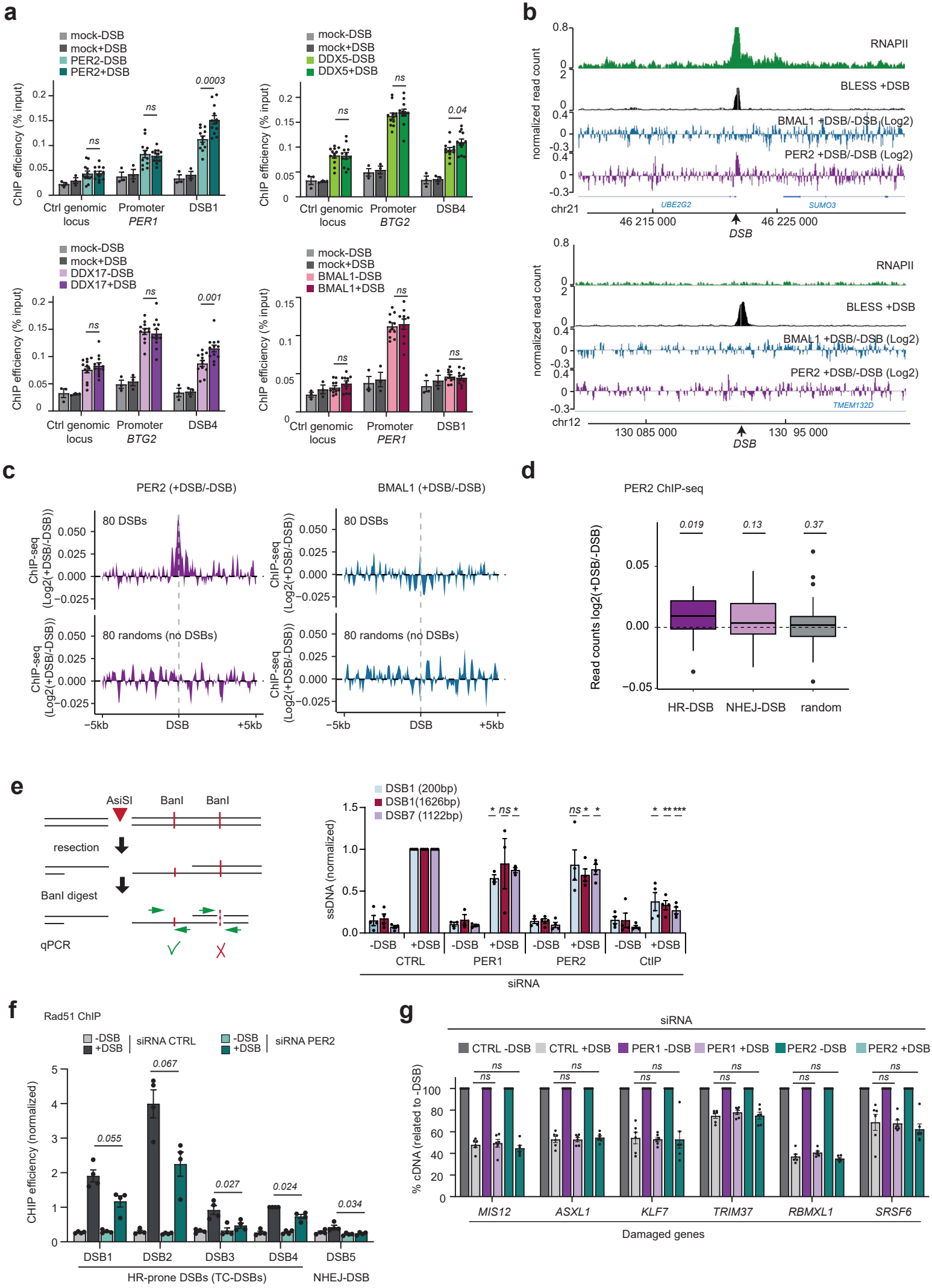
a
mock-DSB
mock+DSB
PER2-DSB
PER2+DSB
ChIP efficiency (% input)
ns
0.0003
Ctrl genomic locus
Promoter PER1
DSB1
DDX5-DSB
DDX5+DSB
0.04
Promoter BTG2
DSB4
DDX17-DSB
DDX17+DSB
0.001
BMAL1-DSB
BMAL1+DSB
b
normalized read count
RNAPII
BLESS +DSB
BMAL1 +DSB/-DSB (Log2)
PER2 +DSB/-DSB (Log2)
UBE2G2
SUMO3
chr21
46 215 000
46 225 000
DSB
TMEM132D
chr12
130 085 000
130 95 000
c
PER2 (+DSB/-DSB)
BMAL1 (+DSB/-DSB)
ChIP-seq (Log2(+DSB/-DSB))
80 DSBs
80 randoms (no DSBs)
−5kb
DSB
+5kb
d
PER2 ChIP-seq
Read counts log2(+DSB/-DSB)
0.019
0.13
0.37
HR-DSB
NHEJ-DSB
random
e
AsiSI
BanI
resection
BanI digest
qPCR
DSB1 (200bp)
DSB1(1626bp)
DSB7 (1122bp)
ssDNA (normalized)
-DSB
+DSB
CTRL
PER1
PER2
CtIP
siRNA
f
Rad51 ChIP
siRNA CTRL
siRNA PER2
CHIP efficiency (normalized)
0.055
0.067
0.027
0.024
0.034
DSB1
DSB2
DSB3
DSB4
DSB5
HR-prone DSBs (TC-DSBs)
NHEJ-DSB
g
siRNA
CTRL -DSB
CTRL +DSB
PER1 -DSB
PER1 +DSB
PER2 -DSB
PER2 +DSB
% cDNA (related to -DSB)
MIS12
ASXL1
KLF7
TRIM37
RBMXL1
SRSF6
Damaged genes

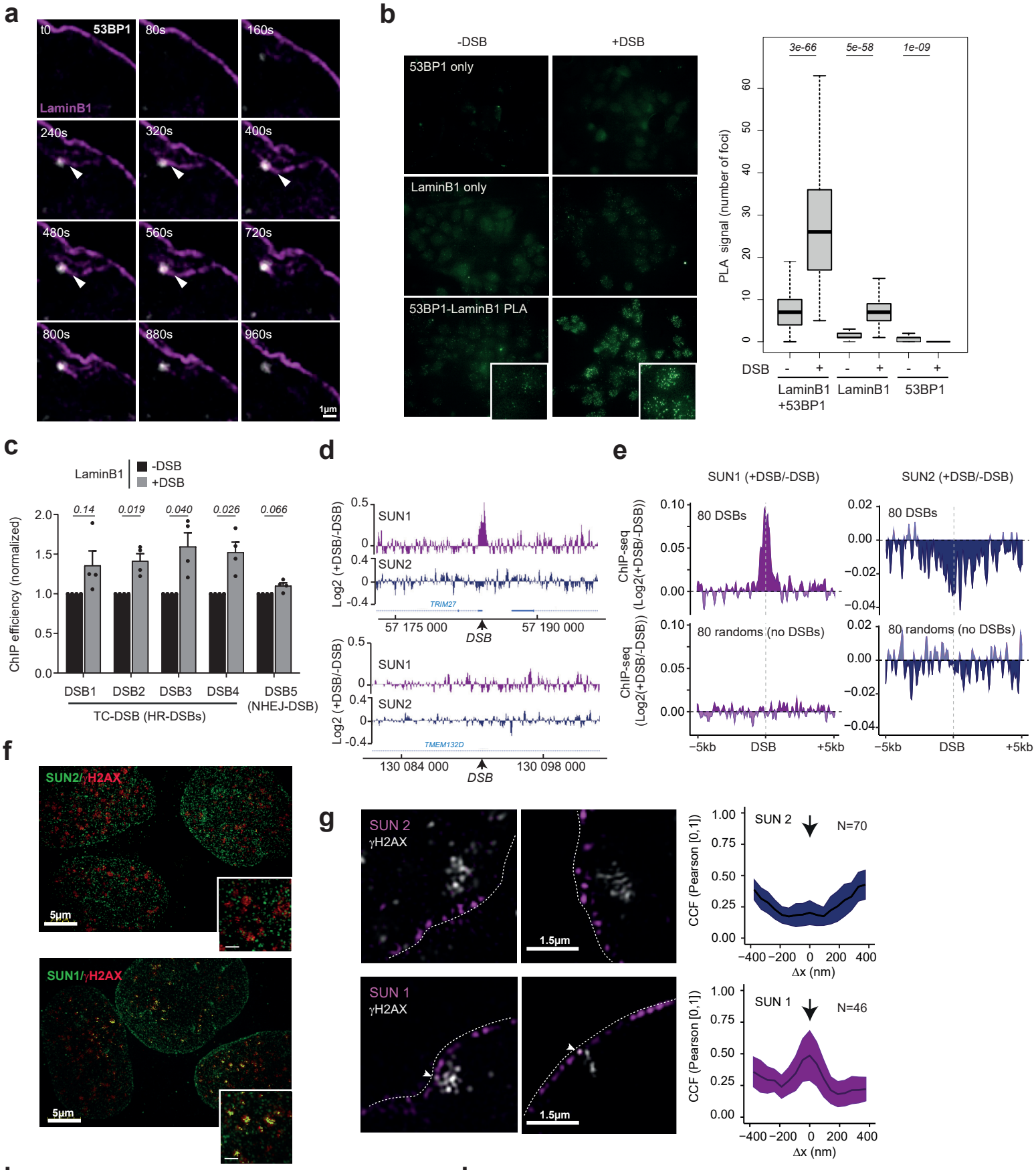
a
t0
53BP1
LaminB1
80s
160s
240s
320s
400s
480s
560s
720s
800s
880s
960s
1µm
b
-DSB
+DSB
53BP1 only
LaminB1 only
53BP1-LaminB1 PLA
3e-66
5e-58
1e-09
PLA signal (number of foci)
DSB
LaminB1 +53BP1
LaminB1
53BP1
c
LaminB1
-DSB
+DSB
ChIP efficiency (normalized)
0.14
0.019
0.040
0.026
0.066
DSB1
DSB2
DSB3
DSB4
DSB5 (NHEJ-DSB)
TC-DSB (HR-DSBs)
d
SUN1
SUN2
Log2 (+DSB/-DSB)
TRIM27
57 175 000
57 190 000
DSB
TMEM132D
130 084 000
130 098 000
e
SUN1 (+DSB/-DSB)
SUN2 (+DSB/-DSB)
ChIP-seq (Log2(+DSB/-DSB))
80 DSBs
80 randoms (no DSBs)
−5kb
DSB
+5kb
f
SUN2/γH2AX
SUN1/γH2AX
5µm
g
SUN 2
γH2AX
SUN 1
1.5µm
CCF (Pearson [0,1])
N=70
N=46
Δx (nm)
h
Cell survival (%)
ns
siRNA
CTRL
SUN1
SUN2
+ DSB
+ DSB + repair
i
Translocation frequency (normalized to CTRL+DSB)
DSB
siRNA
t (MIS12;TRIM37)
t (LINC00271;LYRM2)

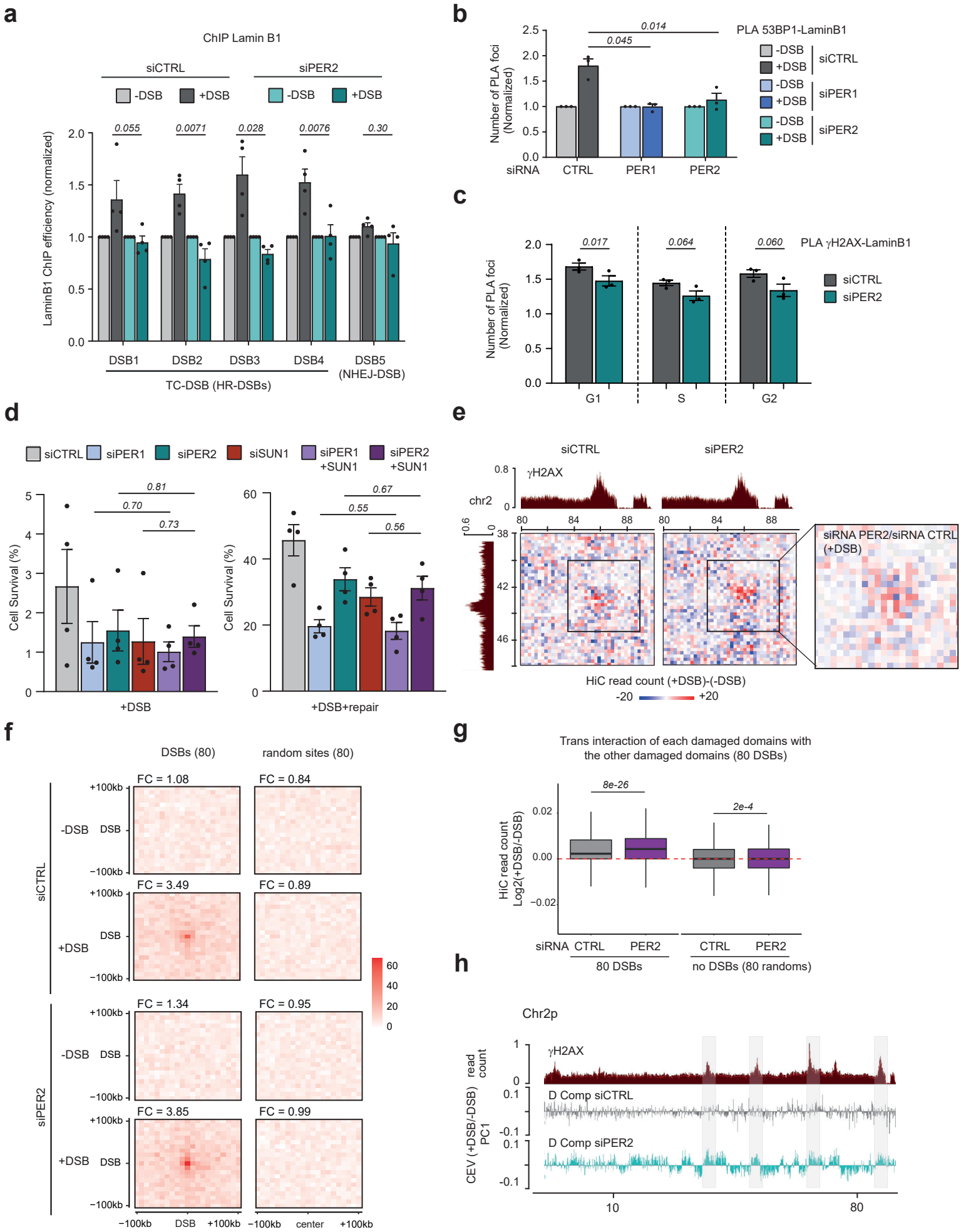
a
ChIP Lamin B1
siCTRL
siPER2
-DSB
+DSB
-DSB
+DSB
LaminB1 ChIP efficiency (normalized)
0.055
0.0071
0.028
0.0076
0.30
DSB1
DSB2
DSB3
DSB4
DSB5 (NHEJ-DSB)
TC-DSB (HR-DSBs)
b
PLA 53BP1-LaminB1
Number of PLA foci (Normalized)
0.014
0.045
siCTRL
siPER1
siPER2
siRNA
CTRL
PER1
PER2
c
PLA γH2AX-LaminB1
Number of PLA foci (Normalized)
0.017
0.064
0.060
siCTRL
siPER2
G1
S
G2
d
siCTRL
siPER1
siPER2
siSUN1
siPER1 +SUN1
siPER2 +SUN1
Cell Survival (%)
0.81
0.70
0.73
+DSB
0.67
0.55
0.56
+DSB+repair
e
siCTRL
siPER2
γH2AX
chr2
siRNA PER2/siRNA CTRL (+DSB)
HiC read count (+DSB)-(-DSB)
-20
+20
f
DSBs (80)
random sites (80)
FC = 1.08
FC = 0.84
FC = 3.49
FC = 0.89
FC = 1.34
FC = 0.95
FC = 3.85
FC = 0.99
siCTRL
siPER2
-DSB
+DSB
+100kb
−100kb
DSB
center
g
Trans interaction of each damaged domains with the other damaged domains (80 DSBs)
HiC read count Log2(+DSB/-DSB)
8e-26
2e-4
siRNA
CTRL
PER2
80 DSBs
no DSBs (80 randoms)
h
Chr2p
read count
γH2AX
D Comp siCTRL
D Comp siPER2
CEV (+DSB/-DSB) PC1
10
80

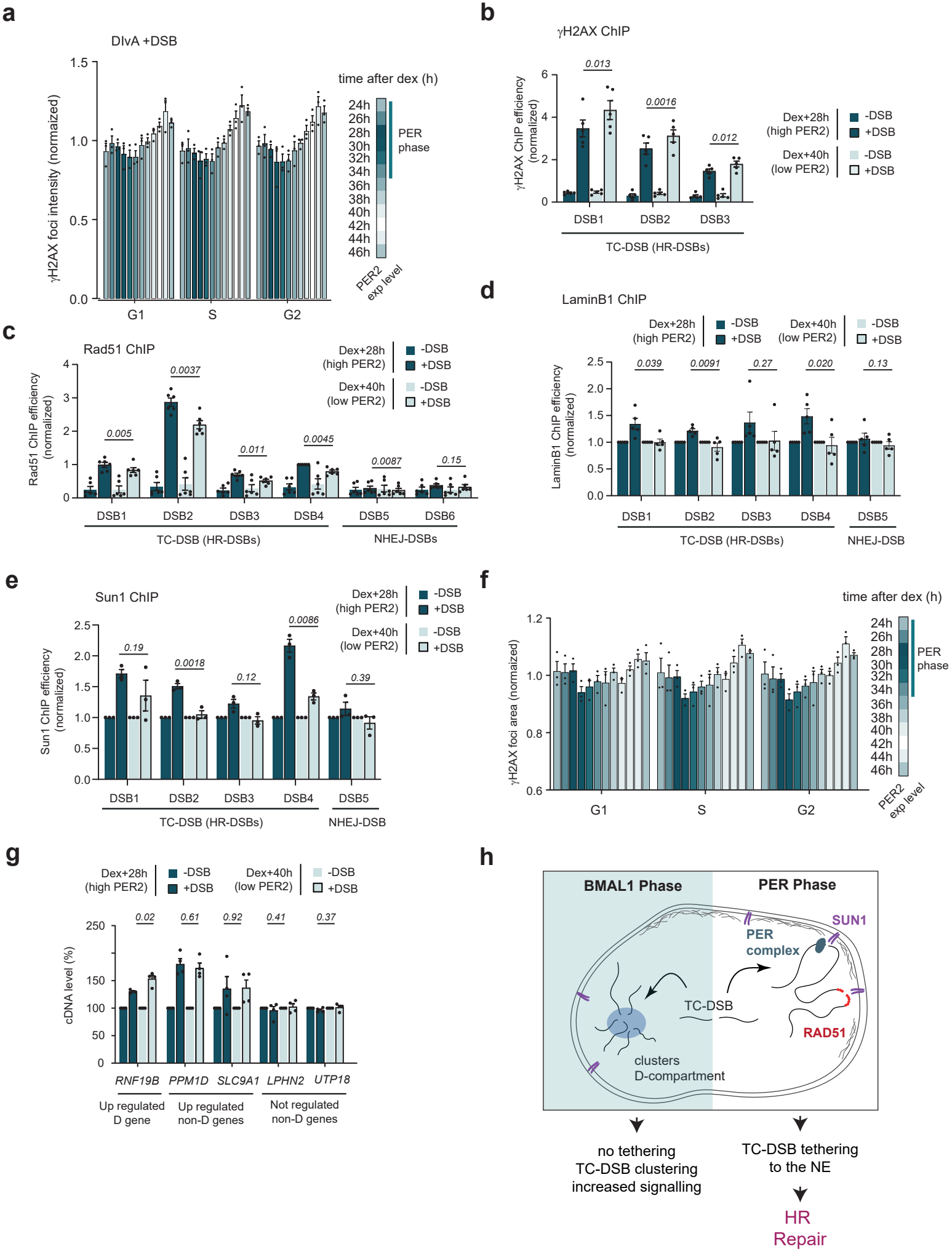
a
DIvA +DSB
γH2AX foci intensity (normalized)
time after dex (h)
24h
26h
28h
30h
32h
34h
36h
38h
40h
42h
44h
46h
PER phase
PER2 exp level
G1
S
G2
b
γH2AX ChIP
γH2AX ChIP efficiency (normalized)
0.013
0.0016
0.012
Dex+28h (high PER2)
-DSB
+DSB
Dex+40h (low PER2)
-DSB
+DSB
DSB1
DSB2
DSB3
TC-DSB (HR-DSBs)
c
Rad51 ChIP
Rad51 ChIP efficiency (normalized)
0.005
0.0037
0.011
0.0045
0.0087
0.15
DSB1
DSB2
DSB3
DSB4
DSB5
DSB6
TC-DSB (HR-DSBs)
NHEJ-DSBs
d
LaminB1 ChIP
LaminB1 ChIP efficiency (normalized)
0.039
0.0091
0.27
0.020
0.13
DSB1
DSB2
DSB3
DSB4
DSB5
TC-DSB (HR-DSBs)
NHEJ-DSB
e
Sun1 ChIP
Sun1 ChIP efficiency (normalized)
0.19
0.0018
0.12
0.0086
0.39
DSB1
DSB2
DSB3
DSB4
DSB5
TC-DSB (HR-DSBs)
NHEJ-DSB
f
γH2AX foci area (normalized)
time after dex (h)
PER phase
PER2 exp level
G1
S
G2
g
cDNA level (%)
0.02
0.61
0.92
0.41
0.37
RNF19B
PPM1D
SLC9A1
LPHN2
UTP18
Up regulated D gene
Up regulated non-D genes
Not regulated non-D genes
h
BMAL1 Phase
PER Phase
SUN1
PER complex
TC-DSB
RAD51
clusters D-compartment
no tethering
TC-DSB clustering
increased signalling
TC-DSB tethering to the NE
HR Repair